Published for SISSA by Springer

Received: June 1, 2021
Revised: September 10, 2021
Accepted: September 16, 2021
Published: October 13, 2021

Measuring Higgs boson self-couplings with $2 \to 3$ VBS processes

Junmou Chen,[a] **Chih-Ting Lu**[b] **and Yongcheng Wu**[c]

[a] *Department of Physics, Jinan University, Guangzhou, Guangdong Province, 510632, China*
[b] *School of Physics, Korean Institute for Advanced Study, Seoul, 02455, Korea*
[c] *Department of Physics, Oklahoma State University, Stillwater, OK 74078, U.S.A.*

E-mail: chenjm@jnu.edu.cn, timluyu@kias.re.kr, ywu@okstate.edu

Abstract: We study the measurement of Higgs boson self-couplings through $2 \to 3$ vector boson scattering (VBS) processes in the framework of Standard Model effective field theory (SMEFT) at both proton and lepton colliders. The SMEFT contribution to the amplitude of the $2 \to 3$ VBS processes, taking $W_L W_L \to W_L W_L h$ and $W_L W_L \to hhh$ as examples, exhibits enhancement with the energy $\frac{\mathcal{A}^{\rm BSM}}{\mathcal{A}^{\rm SM}} \sim \frac{E^2}{\Lambda^2}$, which indicates the sensitivity of these processes to the related dimension-six operators in SMEFT. Simulation of the full processes at both hadron and lepton colliders with a variety of collision energies are performed to estimate the allowed region on c_6 and c_{Φ_1}. Especially we find that, with the help of exclusively choosing longitudinal polarizations in the final states and suitable p_T cuts, WWh process is as important as the more widely studied triple Higgs production (hhh) in the measurement of Higgs self-couplings. Our analysis indicates that these processes can play important roles in the measurement of Higgs self-couplings at future 100 TeV pp colliders and muon colliders. However, their cross sections are generally tiny at low energy machines, which makes them much more challenging to explore.

Keywords: Higgs Physics, Beyond Standard Model, Effective Field Theories

ArXiv ePrint: 2105.11500

Open Access, © The Authors.
Article funded by SCOAP[3].

https://doi.org/10.1007/JHEP10(2021)099

JHEP10(2021)099

Contents

JHEP10(2021)099

1 Introduction

The discovery of Higgs boson at LHC [1, 2] marked a new era for particle physics. Although all experimental results so far agree with the standard model (SM), the origin of electroweak symmetry breaking (EWSB) still remains a mystery and deserves more detailed studies [3–7]. Meanwhile the absence of BSM signal also makes precise measurements of Higgs properties more important than ever. Especially, in order to determine the shape of the Higgs potential, the measurement of Higgs self-couplings becomes critical.

The most straightforward approach to measure Higgs couplings is through direct productions of Higgs boson(s). As the most notable example, the main channel to measure trilinear Higgs self-couplings at the LHC is the di-Higgs production through gluon-gluon fusion, see e.g. [8–15] and references therein. However, processes related to longitudinal vector bosons can also be used for the measurement of Higgs couplings [16, 17]. The underlying reason is as following: according to Goldstone equivalence theorem (GET) [18–20], scattering amplitudes of longitudinal vector bosons can be approximately evaluated by amplitudes of the corresponding Goldstone bosons i.e. $V_L \sim \phi$. Moreover, since Goldstone bosons and the Higgs boson form a SU(2) doublet in the SM, as well as in the Standard Model effective field theory (SMEFT) [21–23], couplings of the Goldstone bosons are related to Higgs couplings through the same parameters. Therefore, processes involving longitudinal vector bosons provide an alternative approach to measure Higgs couplings.

Recently, it was proposed in [16] that vector boson scattering (VBS) processes with multiple final states at the LHC with or even without Higgs involved (and its counterparts at lepton colliders) can be used for the measurement of trilinear Higgs coupling. It was argued that the energy increase of dim-6 operators from longitudinal vector boson enhances the sensitivity of amplitudes to related Wilson coefficients in high energy. As a result, those process can potentially be very beneficial to the precise measurement of Higgs self-couplings. In this work we follow up this proposal by studying $2 \to 3$ VBS processes extensively at different colliders. Different from [16], however, our strategy is to take GET directly and analyze the high energy behavior of $2 \to 3$ VBS amplitudes under SMEFT. The goal of our paper is two folded. First, we try to understand more clearly how higher dimension operators affect the amplitudes of $2 \to 3$ VBS. This is mainly achieved by analyzing how different Feynman diagrams (after taking GET) contribute to the amplitude. We choose $W_L W_L \to W_L W_L h$ and $W_L^+ W_L^- \to hhh$ as examples with $V_L V_L h$ and hhh final states respectively. Second, guided by the results of analyzing amplitudes, we carry out simulations to study the measurement of Higgs self-couplings at the HL-LHC, as well as its future upgrades (HE-LHC), 100 TeV pp colliders and lepton colliders [24–37].[1] We set to give a qualitative picture of the sensitivity of full processes at colliders to dim-6 operators, and the potential of the measurement of Higgs self-couplings at different colliders.

Our main results are briefly summarized as following. At high energy regions, amplitudes of $2 \to 3$ VBS are indeed sensitive to dim-6 operators, with $\frac{\mathcal{A}^{\rm BSM}}{\mathcal{A}^{\rm SM}} \sim \frac{E^2}{\Lambda^2}$. However, there are some subtleties involved that will be discussed carefully in the paper. This sensitivity to dim-6 operators translates further to full processes at colliders, although smallness of cross sections indicates that the processes can only be useful at the future 100 TeV pp colliders or high energy muon colliders. After exclusively selecting longitudinal polarizations for vector bosons in the final states and applying suitable p_T cuts in the phase space of final state particles, processes with final state WWh are found to be as important as triple Higgs production (hhh).

The rest of the paper is organized as following. In section 2, we lay down the framework of SMEFT and discuss the dim-6 operators that are relevant in this paper and then derive and discuss related scalar couplings. Then, we derive and analyze the amplitudes of $W_L W_L \to W_L W_L h$ and $W_L^+ W_L^- \to hhh$ at high energy by using GET in section 3. The dependence on Wilson coefficients are also discussed, along with other subtleties. The cross section for the full processes $pp \to jj W_L W_L h$ and $pp \to jjhhh$ at hadron colliders and $\mu^+\mu^- \to \nu_\mu \overline{\nu}_\mu W_L^+ W_L^- h$ and $\mu^+\mu^- \to \nu_\mu \overline{\nu}_\mu hhh$ at muon colliders are studied in section 4 through which we discuss the sensitivity of these channels on the SMEFT operators. Finally, we conclude in section 5.

[1] Some previous studies for exploring trilinear Higgs coupling can be found in [38–50].

JHEP10(2021)099

2 Scalar couplings in SMEFT

2.1 Relevant Dim-6 operators in SMEFT

The null result of searching BSM signals at the LHC indicates that new physics may be hidden at the energy scale much higher than the electroweak (EW) scale. This justifies the usage of effective field theory (EFT) to constrain the possible new physics in a model independent way. Preserving the SM gauge symmetry group of $\mathrm{SU}(3)_c \times \mathrm{SU}(2)_L \times \mathrm{U}(1)_Y$ further reduces the framework to SMEFT. This framework is suitable for the scenario that the Higgs boson is an elementary particle [6]. We will focus on this case and ignore other exotic scenarios hereafter.

Generally, if we ignore the dim-5 Weinberg operator [21], the Lagrangian for SMEFT can be written as

$$\mathcal{L} = \mathcal{L}_{\mathrm{SM}} + \sum_i \frac{c_i \mathcal{O}_i}{\Lambda^2} + \mathcal{O}\left(\frac{1}{\Lambda^3}\right) \tag{2.1}$$

The first term $\mathcal{L}_{\mathrm{SM}}$ is the Lagrangian for the SM, which includes all known physics; the second term includes all dim-6 operators that are suppressed by Λ^2, with Λ being the energy scale of new physics and c_i being Wilson coefficients of the corresponding operators $\mathcal{O}_i$.

Ignoring CP violating terms, dim-6 operators relevant to couplings of (and between) scalars and gauge bosons can be written as

$$\begin{aligned}\mathcal{L}_{\mathrm{dim-6}} = \frac{1}{\Lambda^2}\Big(& c_6(\Phi^\dagger\Phi)^3 + c_{\Phi_1}\partial^\mu(\Phi^\dagger\Phi)\partial_\mu(\Phi^\dagger\Phi) + c_{\Phi_2}(\Phi^\dagger D^\mu\Phi)^*(\Phi^\dagger D_\mu\Phi) \\ & + c_{\Phi^2W^2}\Phi^\dagger\Phi W^a_{\mu\nu}W^{a\mu\nu} + c_{\Phi^2B^2}\Phi^\dagger\Phi B_{\mu\nu}B^{\mu\nu} + c_{\Phi^2WB}\Phi^\dagger\tau^a\Phi W^a_{\mu\nu}B^{\mu\nu} \\ & + c_{W^3}\epsilon^{abc}W^{a\nu}_\mu W^{b\rho}_\nu W^{b\mu}_\rho\Big)\end{aligned} \tag{2.2}$$

where Φ is the Higgs doublet and can be parameterized as

$$\Phi = \begin{pmatrix} \phi^+ \\ \frac{v+h+i\phi^0}{\sqrt{2}} \end{pmatrix} \tag{2.3}$$

The processes considered in this paper are $2 \to 3$ VBS with initial and final vector bosons being longitudinal polarized, $V_LV_L \to V_LV_Lh$ and $V_LV_L \to hhh$. In general, after EWSB, $\phi^\pm/\phi^0$ are considered as unphysical, "eaten" by gauge fields $W^\pm/Z$ becoming their longitudinal components. The "real" identities of those degrees of freedom only reveal themselves at high energy through GET [18–20, 51–56]. Especially in unitary gauge, Φ becomes $\Phi = \left(0, (v+h)/\sqrt{2}\right)^T$ under which the would-be Goldstone bosons disappear from the physical spectrum and Feynman diagrams. The three operators in the first line of eq. (2.2), $\mathcal{O}_6$, $\mathcal{O}_{\Phi_1}$ and $\mathcal{O}_{\Phi_2}$, induce and modify Higgs self-couplings, as well as couplings between vector boson bosons and the Higgs boson. The operators in the second line and the third line in eq. (2.2) are also involved in scatterings of longitudinal vector bosons, because in this physical picture, couplings involving longitudinal vector bosons, especially vector bosons couplings to vector bosons, are mainly induced by gauge fields. However, there is a well-known problem in this physical picture of only gauge bosons being physical: power counting becomes invalid. This becomes a major obstacle to understanding the

JHEP10(2021)099

leading energy behavior of processes involving longitudinal vector bosons. Especially, in the presence of SMEFT, higher dimensional operators usually have derivative couplings that lead to unitarity violating energy increase of S-matrix which are suppressed by scale Λ. Meanwhile, longitudinal polarization vectors also bring energy increase in the diagram by diagram level, which nevertheless disappears in the final S-matrix as guaranteed by GET. The real energy increase from derivative couplings and spurious energy increase from longitudinal vector bosons mix together in unitary gauge and the related physical picture. This obscures the underlying physics greatly.

To solve the problem discussed above, we simply take GET and identify V_L with ϕ directly. This is a good approximation as long as the energy scale is much larger than EW scale. Without the spurious energy increase from longitudinal polarization vectors, the energy behavior of Feynman diagrams becomes physical. Thus we can analyze the amplitudes at the level of single diagrams and obtain the leading energy behavior of the processes. Moreover, since $\phi^{\pm}/\phi^0$ and h all belong to the same SU(2) Higgs doublet, the couplings of (and between) Goldstone bosons and Higgs boson, are determined by the same parameters of the Higgs potential. Thus it becomes manifest that we can measure Higgs self-couplings through processes involving V_Ls or ϕs.

Now let's review the dim-6 operators in eq. (2.2) under GET. Higgs self-couplings and couplings between Goldstone bosons and Higgs are induced by $\mathcal{O}_6$, $\mathcal{O}_{\Phi_1}$ and $\mathcal{O}_{\Phi_2}$, together with SM Lagrangian terms. $\mathcal{O}_6$ is the only one that contributes to 5-point and 6-point scalar vertices. $\mathcal{O}_{\Phi_2}$ term violates custodial symmetry, the Wilson coefficient c_{Φ_2} is strongly constrained by LEP [39]. Therefore, we will ignore it from now on. $\mathcal{O}_{\Phi_1}$, $\mathcal{O}_{\Phi^2W^2}$, $\mathcal{O}_{\Phi^2B^2}$ and $\mathcal{O}_{\Phi^2WB}$ give rise to gauge-gauge-scalar and gauge-gauge-scalar-scalar vertices. $\mathcal{O}_{W^3}$ doesn't contribute to $V_LV_L \to V_LV_Lh$, but can have contributions to the amplitudes if the polarizations of vector bosons are transverse. Moreover, $\mathcal{O}_{W^3}$'s vertices also contribute to $2 \to 4$ process, e.g. $V_LV_L \to V_LV_Lhh$. For simplicity, we are only interested in the modification to scalar couplings in this work. Thus only $\mathcal{O}_6$ and $\mathcal{O}_{\Phi_1}$ are considered.

2.2 Scalar vertices

The full Feynman rules in SMEFT can be found in [57]. Here we briefly review the results related to our processes. Before symmetry breaking, the Lagrangian in scalar sector is

$$\mathcal{L}_\Phi = (D_\mu\Phi)^\dagger(D^\mu\Phi) + \mu^2\Phi^\dagger\Phi - \lambda_h(\Phi^\dagger\Phi)^2 + \frac{c_6}{\Lambda^2}(\Phi^\dagger\Phi)^3 + \frac{c_{\Phi_1}}{\Lambda^2}\partial^\mu(\Phi^\dagger\Phi)\partial_\mu(\Phi^\dagger\Phi), \tag{2.4}$$

where Λ is the new physics scale, which we choose as 1 TeV in the paper. After symmetry breaking, the VEV v can be expressed in terms of μ, λ_h and c_6 by tracking the minimum position of the Higgs potential,

$$v = \sqrt{\frac{\mu^2}{\lambda_h}} - \frac{3}{8}\frac{\mu^3}{\lambda_h^{5/2}}\frac{c_6}{\Lambda^2} \tag{2.5}$$

The Higgs field h and goldstone field ϕ^0 need extra field renormalization, after which, we obtain Higgs mass m_h in terms of $(v, c_6, c_{\Phi_1}, \lambda_h)$:

$$m_h^2 = \frac{1}{2}\lambda_h v^2 - (3c_6 + \lambda_h c_{\Phi_1})\frac{v^4}{\Lambda^2} \tag{2.6}$$

JHEP10(2021)099

Eliminating (μ, λ_h) by (m_h, v) through eq. (2.5) and eq. (2.6), we can express all scalar vertices in terms of $(m_h, v, c_6, c_{\Phi_1})$, with $v^2 = \frac{\sqrt{2}g}{2G_F} \approx (246\,\text{GeV})^2$. Then, we have all 3-point, 4-point and 5-point scalar couplings to be

$$\lambda_{h\phi^+\phi^-} = \lambda_{h\phi^0\phi^0} = -i\frac{m_h^2}{v} + ic_{\Phi_1} v \frac{2p_h^2 + m_h^2}{\Lambda^2}, \tag{2.7a}$$

$$\lambda_{hhh} = -i\left(\frac{3m_h^2}{v} - 6c_6\frac{v^3}{\Lambda^2}\right) + ic_{\Phi_1} v \frac{2p_1^2 + 2p_2^2 + 2p_3^2 + 3m_h^2}{\Lambda^2}, \tag{2.7b}$$

$$\lambda_{\phi_0^4} = -3i\frac{m_h^2}{v^2} - 3ic_{\Phi_1}\frac{v^2}{\Lambda^2} - 2ic_{\Phi_1}\frac{(p_1+p_2)^2 + (p_1+p_3)^2 + (p_1+p_4)^2}{\Lambda^2}, \tag{2.7c}$$

$$\lambda_{\phi_+\phi_-\phi_0^2} = -i\frac{m_h^2}{v^2} - ic_{\Phi_1}\frac{v^2}{\Lambda^2} - 2ic_{\Phi_1}\frac{(p_1+p_2)^2}{\Lambda^2}, \tag{2.7d}$$

$$\begin{aligned}\lambda_{\phi_+^2\phi_-^2} &= -2i\frac{m_h^2}{v^2} - 2ic_{\Phi_1}\frac{v^2}{\Lambda^2} \\ &\quad - 2ic_{\Phi_1}\frac{2(p_1+p_3)^2 + 2(p_1+p_4)^2 - p_1^2 - p_2^2 - p_3^2 - p_4^2}{\Lambda^2},\end{aligned} \tag{2.7e}$$

$$\lambda_{\phi_+\phi_- h^2} = \lambda_{\phi_0^2 h^2} = -i\left(\frac{m_h^2}{v^2} - 6c_6\frac{v^2}{\Lambda^2} + c_{\Phi_1}\frac{v^2}{\Lambda^2}\right) - 2ic_{\Phi_1}\frac{(p_1+p_2)^2 + m_h^2}{\Lambda^2}, \tag{2.7f}$$

$$\begin{aligned}\lambda_{h^4} &= -3i\left(\frac{m_h^2}{v^2} - 12c_6\frac{v^2}{\Lambda^2} + c_{\Phi_1}\frac{v^2}{\Lambda^2}\right) \\ &\quad - 2ic_{\Phi_1}\frac{(p_1+p_2)^2 + (p_1+p_3)^2 + (p_1+p_4)^2 + 6m_h^2}{\Lambda^2},\end{aligned} \tag{2.7g}$$

$$\lambda_{\phi^+\phi^- h^3} = \lambda_{(\phi^0)^2 h^3} = \lambda_{(\phi^0)^4 h} = 18ic_6\frac{v}{\Lambda^2}, \tag{2.7h}$$

$$\lambda_{(\phi^+\phi^-)^2 h} = 12ic_6\frac{v}{\Lambda^2}, \tag{2.7i}$$

$$\lambda_{\phi^+\phi^-(\phi^0)^2 h} = 6ic_6\frac{v}{\Lambda^2}, \tag{2.7j}$$

where p_h in $\lambda_{h\phi^+\phi^-}$ and $\lambda_{h\phi^0\phi^0}$ is the momentum of the Higgs boson; p_1, p_2 in $\lambda_{\phi_+\phi_-\phi_0^2}$, $\lambda_{\phi_+\phi_- h^2}$ and $\lambda_{\phi_0^2 h^2}$ are momenta of ϕ^+/ϕ^- or equivalently h; in $\lambda_{\phi_+^2\phi_-^2}$, we can assign p_1 and p_2 to ϕ^+, p_3 and p_4 to ϕ^-. 6-point scalar couplings are not listed as they are irrelevant to the processes we study here.

3 Amplitudes and cross sections

3.1 Feynman diagrams and amplitudes with Goldstone equivalence

In this section we analyze the amplitude of $V_L V_L \to V_L V_L h$ and $V_L V_L \to hhh$ at high energy by using GET for SM plus two dim-6 operators of SMEFT ($\mathcal{O}_6$, $\mathcal{O}_{\Phi_1}$). For simplicity, we will choose $W_L^+ W_L^- \to W_L^+ W_L^- h$ and $W_L^+ W_L^- \to hhh$ as examples to illustrate the general behavior, and work in Feynman gauge.

Following GET, $W_L^+ W_L^- \to W_L^+ W_L^- h$ and $W_L^+ W_L^- \to hhh$ can be approximated by $\phi^+(p_1)\phi^-(p_2) \to \phi^+(p_3)\phi^-(p_4)h(p_5)$ and $\phi^+(p_1)\phi^-(p_2) \to h(p_3)h(p_4)h(p_5)$ at high energy. The corresponding amplitudes can be classified according to the number of propagators:

JHEP10(2021)099

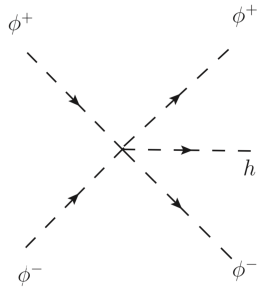

Figure 1. Contact diagram for $\phi^+\phi^- \to \phi^+\phi^- h$.

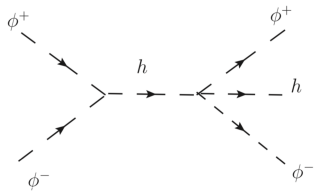

Figure 2. A typical diagram with one propagator for $\phi^+\phi^- \to \phi^+\phi^- h$.

zero, one or two propagators:

$$\mathcal{A} = \mathcal{A}_0 + \mathcal{A}_1 + \mathcal{A}_2, \tag{3.1}$$

where $\mathcal{A}_i$ with $i = 0, 1, 2$ can be further classified as diagrams from SM vertices only and diagrams including BSM contributions: $\mathcal{A}_i = \mathcal{A}_i^{\rm SM} + \mathcal{A}_i^{\rm BSM}$.

Before going to the analysis in details, it's important to understand in a general way how the high energy behavior of $\phi\phi \to \phi\phi h$ is determined. After the unphysical energy increase from longitudinal polarization vectors getting eliminated, physical energy dependence only comes from derivative couplings in dim-6 operators as well as the $\frac{1}{E^2}$ factor of the propagators. Understanding the overall energy behavior of the amplitude from the interplay of different factors is the main focus of our analysis. We mainly focus on $\phi^+\phi^- \to \phi^+\phi^- h$ process, and make comments when there is difference with $\phi^+\phi^- \to hhh$. Since we will focus on the high energy behavior, we also only keep the leading terms in $\frac{1}{E}$. For $\mathcal{A}^{\rm BSM}$, we only keep the leading terms of $\frac{c_i}{\Lambda^2}$. Higher order terms of $\frac{1}{\Lambda^2}$ are neglected as they are suppressed by additional powers of Λ. Moreover, to be fully consistent when considering higher order terms, we would have to take into account the higher dimensional operators, thus go beyond dim-6 SMEFT.

Diagrams with 0 propagator. In the SM, $\phi^+\phi^- \to \phi^+\phi^- h$ and $\phi^+\phi^- \to hhh$ have no 5-point contact diagram. There is, however, one such diagram from the $\mathcal{O}_6$ operator, as shown in figure 1. The corresponding amplitudes are

$$\mathcal{A}_0^{\phi^+\phi^-\to\phi^+\phi^- h} = \lambda_{(\phi^+\phi^-)^2 h} = 12ic_6\frac{v}{\Lambda^2} \tag{3.2}$$

$$\mathcal{A}_0^{\phi^+\phi^-\to hhh} = \lambda_{\phi^+\phi^- h^3} = 18ic_6\frac{v}{\Lambda^2} \tag{3.3}$$

In both cases we obtain $\mathcal{A}_0 \sim \frac{v}{\Lambda^2}$.

JHEP10(2021)099

Diagrams with 1 propagator. For any $2 \to 3$ process, the amplitude of all Feynman diagrams with one propagator can be schematically written as

$$\mathcal{A}_1 = \sum_{\text{diagrams}} i\frac{M_4' \cdot M_3'}{q^2 - m^2} \tag{3.4}$$

The intermediate particle of the propagator can be either a scalar or a vector boson, as illustrated in figure 2 for $\phi^+\phi^- \to \phi^+\phi^- h$. M_4' and M_3' denote the amplitudes involving 4-point and 3-point vertices respectively, with Lorentz indices suppressed if the intermediate state is a vector boson. However, for the vector boson propagator, we need $\phi\phi\phi V$-like vertex, which does not exist in the SM and dim-6 operators we consider in this work ($\mathcal{O}_6$ and $\mathcal{O}_{\Phi_1}$).[2] Thus the propagator can only be a scalar.

For SM-only diagrams, we have

$$\begin{aligned}\mathcal{A}_1^{\text{SM}} = &-2i\frac{m_h^2}{v^3}\left(\frac{1}{(p_3+p_5)^2-m_W^2}+\frac{1}{(p_4+p_5)^2-m_W^2}+\frac{1}{(p_2-p_5)^2-m_W^2}+\frac{1}{(p_1-p_5)^2-m_W^2}\right)\\ &-2i\frac{m_h^2}{v^3}\left(\frac{1}{(p_1+p_2)^2-m_h^2}+\frac{1}{(p_1-p_3)^2-m_h^2}\right).\end{aligned} \tag{3.5}$$

Neither 4-point vertices nor 3-point vertices have any energy dependence. Since at high energy, $p_i^2 \sim E^2 \gg m_W^2, m_h^2$, the amplitude scales as $\mathcal{A}_1^{SM} \sim \frac{v}{E^2}$.

For BSM contributions, keep terms up to $\frac{1}{\Lambda^2}$, we have:

$$\begin{aligned}\mathcal{A}_1^{BSM} \simeq &-i2c_{\Phi_1}\frac{m_h^2}{v\Lambda^2}\left(\frac{(p_1+p_2)^2}{(p_4+p_5)^2-m_W^2}+\frac{(p_1+p_2)^2}{(p_3+p_5)^2-m_W^2}+\frac{(p_1-p_3)^2}{(p_2-p_5)^2-m_W^2}+\frac{(p_2-p_4)^2}{(p_1-p_5)^2-m_W^2}\right)\\ &-ic_{\Phi_1}\frac{m_h^2}{v\Lambda^2}\left(\frac{(p_1+p_2)^2}{(p_3+p_4)^2-m_h^2}+\frac{(p_3+p_4)^2}{(p_1+p_2)^2-m_h^2}+\frac{(p_1-p_3)^2}{(p_2-p_4)^2-m_h^2}+\frac{(p_2-p_4)^2}{(p_1-p_3)^2-m_h^2}\right)\\ &-16ic_{\Phi_1}\frac{m_h^2}{v\Lambda^2}\left(\frac{(p_3+p_4)^2}{(p_3+p_4)^2-m_h^2}+\frac{(p_1+p_2)^2}{(p_1+p_2)^2-m_h^2}+\frac{(p_2-p_4)^2}{(p_2-p_4)^2-m_h^2}+\frac{(p_1-p_3)^2}{(p_1-p_3)^2-m_h^2}\right),\end{aligned} \tag{3.6}$$

where both 3-point and 4-point scalar vertices provide momentum-dependent couplings leading to E^2 behavior in the numerator, which cancels the $\frac{1}{E^2}$ factor from the propagator. Therefore, we obtain $\mathcal{A}_1^{BSM} \sim \frac{v}{\Lambda^2}$. Similarly, the behavior of amplitude for $\phi^+\phi^- \to hhh$ also scales as $\frac{v}{E^2}$ in the SM and $\frac{v}{\Lambda^2}$ when dim-6 operators are involved.

Diagrams with 2 propagators. The amplitudes for the Feynman diagrams with two propagators can be classified according to the type of the propagators as shown in figure 3:

(a) Two scalars

(b) One scalar and one vector boson

(c) Two vector bosons

[2] We could have $\phi\phi\phi V$-like vertex, once we include more operators in SMEFT, e.g. $\mathcal{O}_{\Phi_2}$. The analysis will be similar and they have same behavior at high energy.

JHEP10(2021)099

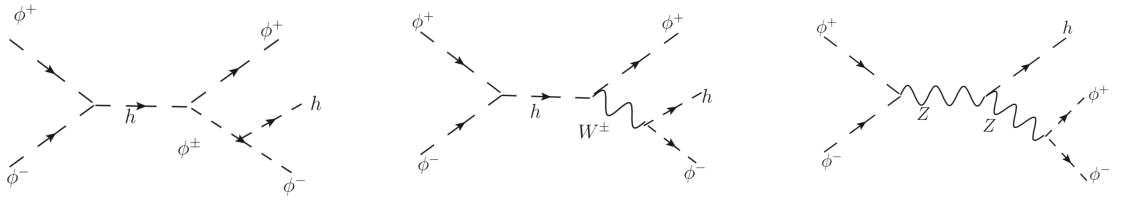

(a) Two scalar propagators.

(b) One scalar propagator, one gauge propagator.

(c) Two gauge propagators.

Figure 3. Typical Diagrams with two propagators for $\phi^+\phi^- \to \phi^+\phi^- h$.

There are too many diagrams with two propagators to give a short and concise analytical expression even in high energy limit, hence we only analyze a representative diagram for each case.

For the case with two scalar propagators, a typical diagram is shown in figure 3a which has both SM and BSM contributions:

$$\begin{aligned}\mathcal{A}_2^{a,\mathrm{SM}} &\simeq -i\left(\frac{m_h^2}{v}\right)^3 \frac{1}{(p_1+p_2)^2-m_h^2}\frac{1}{(p_4+p_5)^2-m_W^2},\\ \mathcal{A}_2^{a,\mathrm{BSM}} &\simeq 4ic_{\Phi_1}\frac{m_h^4}{v\Lambda^2}\frac{(p_1+p_2)^2}{(p_1+p_2)^2-m_h^2}\frac{1}{(p_4+p_5)^2-m_W^2}.\end{aligned} \tag{3.7}$$

Thus, at high energy, diagrams with two scalar propagators scale as $\mathcal{A}_2^{a,\mathrm{SM}} \sim \frac{v^3}{E^4}$, $\mathcal{A}_2^{a,\mathrm{BSM}} \sim \frac{v^3}{\Lambda^2 E^2}$. They are suppressed by $\frac{1}{E^2}$ compared with $\mathcal{A}_1^{\mathrm{SM}}$ and $\mathcal{A}_1^{\mathrm{BSM}}$ respectively.

The typical diagram for the case with one scalar and one vector boson propagators is shown in figure 3b. Summing the diagram and the diagram by exchanging $p_3 \leftrightarrow p_4$, keeping only the leading contributions, we have

$$\mathcal{A}_2^{b,\mathrm{SM}} \simeq i\frac{g^2 m_h^2}{4v}\left(\frac{(p_1+p_2+p_3)(p_5-p_4)}{((p_1+p_2)^2-m_h^2)((p_4+p_5)^2-m_W^2)}+\frac{(p_1+p_2+p_4)(p_5-p_3)}{((p_1+p_2)^2-m_h^2)((p_3+p_5)^2-m_W^2)}\right), \tag{3.8}$$

where we only have SM contribution. At high energy, the amplitude scales as $\mathcal{A}_2^{b,SM} \sim \frac{v}{E^2}$, which is of the same order as $\mathcal{A}_1^{\mathrm{SM}}$.

In figure 3c, we show the typical diagram for the case with two vector boson propagators. The amplitude only receives SM contributions and reads:

$$\mathcal{A}_2^c \simeq= -i\frac{g^3 m_Z c_{2W}^2}{4c_W^3}\frac{(p_1-p_2)\cdot(p_3-p_4)}{((p_1+p_2)^2-m_Z^2)((p_3+p_4)^2-m_Z^2)}, \tag{3.9}$$

where $c_{2W} = \cos 2\theta_W$, $c_W = \cos\theta_W$ and θ_W is the Weinberg angle. At high energy, it scales as $\mathcal{A}_2^c \sim \frac{v}{E^2}$.

Combined amplitudes. Taking into account all cases discussed above, the amplitude of $W_L^+W_L^- \to W_L^+W_L^- h$ can be written as

$$\mathcal{A}(W_L^+W_L^- \to W_L^+W_L^- h) = \mathcal{A}^{\mathrm{SM}} + \mathcal{A}^{\mathrm{BSM}}, \tag{3.10}$$

JHEP10(2021)099

with $\mathcal{A}^{\rm SM}$ being the SM contribution which has no dependence on c_6 or c_{Φ_1} and $\mathcal{A}^{\rm BSM}$ the BSM contributions depending on c_6 and c_{Φ_1}. We only keep the terms up to the order of $\frac{c_i}{\Lambda^2}$, higher order terms are truncated to be consistent with the EFT expansions.

The leading energy dependence of SM and BSM contributions are

$$\mathcal{A}^{\rm SM} \sim \frac{v}{E^2}, \quad \mathcal{A}^{\rm BSM} \sim \frac{v}{\Lambda^2}. \tag{3.11}$$

Thus, the ratio between BSM and SM is approximately

$$\frac{\mathcal{A}^{BSM}}{\mathcal{A}^{SM}} \sim \frac{E^2}{\Lambda^2}. \tag{3.12}$$

From eq. (3.12) we find that, the BSM contribution to the total amplitude will be enhanced relative to the SM one at high energy. Let's stop and analyze the physical reasons behind eq. (3.12). By a naive dimensional analysis, the amplitude for $2 \to 3$ process will scale as $1/(\text{GeV})$. For the SM contributions, combining the energy dependence from the propagator and 3-point vertices, it scales as $\frac{v}{E^2}$ with the energy coming from the propagator. On the other hand, the BSM contribution has a different leading energy behavior — it remains constant as $(\frac{v}{\Lambda^2})$ due to: (a) 5-point scalar vertices as shown in figure 1 from $\mathcal{O}_6$, giving dependence on c_6; (b) The cancellation between energy suppression from propagators and energy increase from momentum dependence in 3/4-point vertices from $\mathcal{O}_{\Phi_1}$, giving dependence on c_{Φ_1}. Although this enhancement of the BSM contribution from c_{Φ_1} relative to SM one applies to many processes, it is not the case for c_6, which depends crucially on the 5-point scalar vertices coming solely from $\mathcal{O}_6$. Since $\mathcal{O}_6$ is also the only source for 6-point scalar vertices, this sensitivity of amplitude to BSM physics for c_6 also applies to $2 \to 4$ VBS processes. In comparison, 4-point scalar vertices can come from both SM and higher dimensional operators, therefore the amplitude of $2 \to 2$ VBS does not have the behavior of eq. (3.11) for c_6.

There is also a subtlety that's related to the so-called soft-collinear singularities that originate from propagators reaching (close to) to the poles, see, for example, [58–63].

After integrating over phase space, those singularities result in logarithmic enhancement to the cross sections which will change the behavior in eq. (3.12) and can reduce the sensitivities to the Wilson coefficients. Hence those singularities require careful treatments which we will discuss in the next section.

3.2 Cross sections for subprocesses

After deriving the amplitudes of $W_LW_L \to W_LW_Lh$ and $W_LW_L \to hhh$ using GET, we will now examine the behaviors of the cross sections for $W_LW_L \to W_LW_Lh$ and $W_LW_L \to hhh$ which is calculated using `FeynArts` [64] and `FormCalc` [65] with a cut $p_T > 50\,\text{GeV}$ on the final states and also cross checked with `MadGraph` [66]. The dependence on c_6 and c_{Φ_1} are considered separately.

The dependence of the cross section for $WW \to WWh$ and $WW \to hhh$ on c_6 is shown in figure 4 for two representative energy $\sqrt{s} = 1\,\text{TeV}$ (solid lines) and $\sqrt{s} = 3\,\text{TeV}$ (dashed lines). The dependence on c_6 for these processes only comes from the 5-point contact terms

JHEP10(2021)099

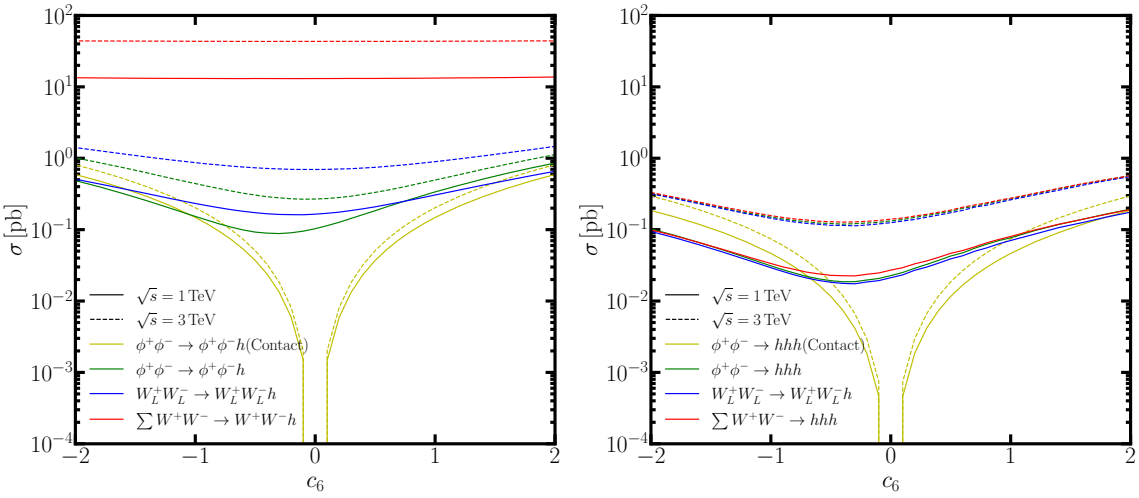

Figure 4. $\hat{\sigma}(W_L^+W_L^- \to W_L^+W_L^- h)$ and $\hat{\sigma}(W_L^+W_L^- \to hhh)$ as functions of c_6.

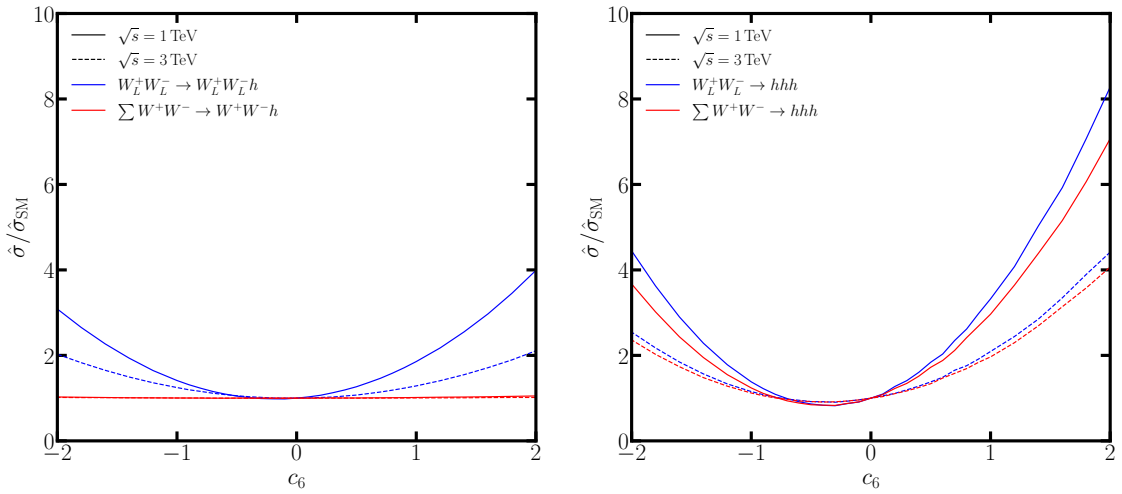

Figure 5. $\hat{\sigma}/\hat{\sigma}_{\text{SM}}$ for $W^+W^- \to W^+W^- h$ and $W^+W^- \to hhh$ as functions of c_6.

as shown in figure 1 which is denoted as the yellow line in figure 4. Thus the dependence of the cross section of $\phi\phi \to \phi\phi h$ and $\phi\phi \to hhh$ (green lines), as well as $W_LW_L \to W_LW_Lh$ and $W_LW_L \to hhh$ (blue lines), mainly follows the behavior of the yellow lines, except the region where c_6 is close to zero.

However, $WW \to WWh$ is dominated by transverse polarizations as can be seen by comparing the red and blue lines. Thus, in order for the former process to remain sensitive to c_6, longitudinal polarizations of W boson pair need to be singled out by some specific selections. The technical details can be found in [67–71]. On the other hand $WW \to hhh$ is dominated by longitudinal polarizations, hence, the sensitivity is largely remained in this sense. In figure 5, we show the ratio $\sigma/\sigma_{\text{SM}}$ as functions of c_6 for $W^+W^- \to W^+W^-h$ and $W^+W^- \to hhh$. It is clear that, by just looking at these $2 \to 3$ processes, $WW \to hhh$ is more sensitive than $WW \to WWh$ on c_6. Note that, the sensitivity is reduced at

JHEP10(2021)099

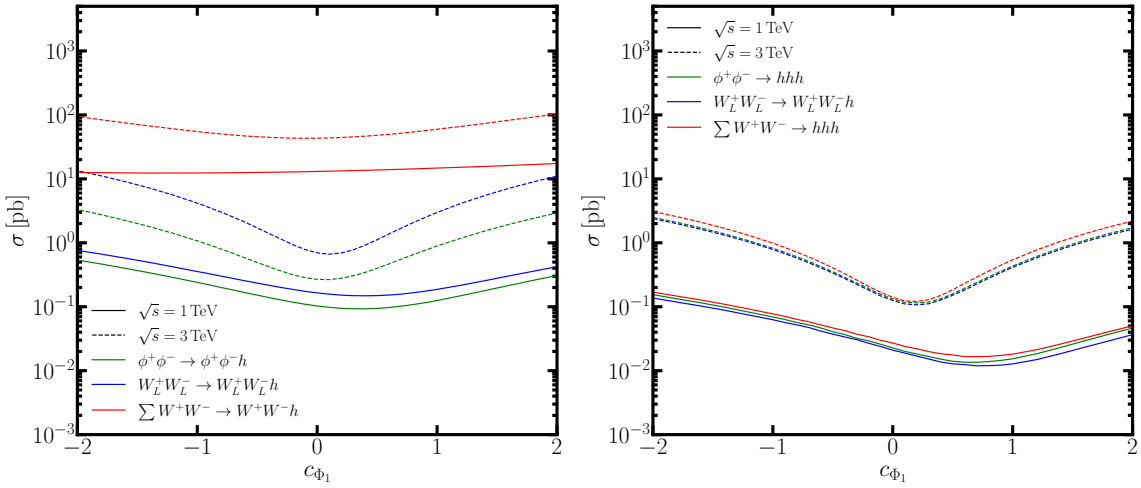

Figure 6. $\hat{\sigma}(W_L^+W_L^- \to W_L^+W_L^- h)$ and $\hat{\sigma}(W_L^+W_L^- \to hhh)$ as functions of c_{Φ_1}.

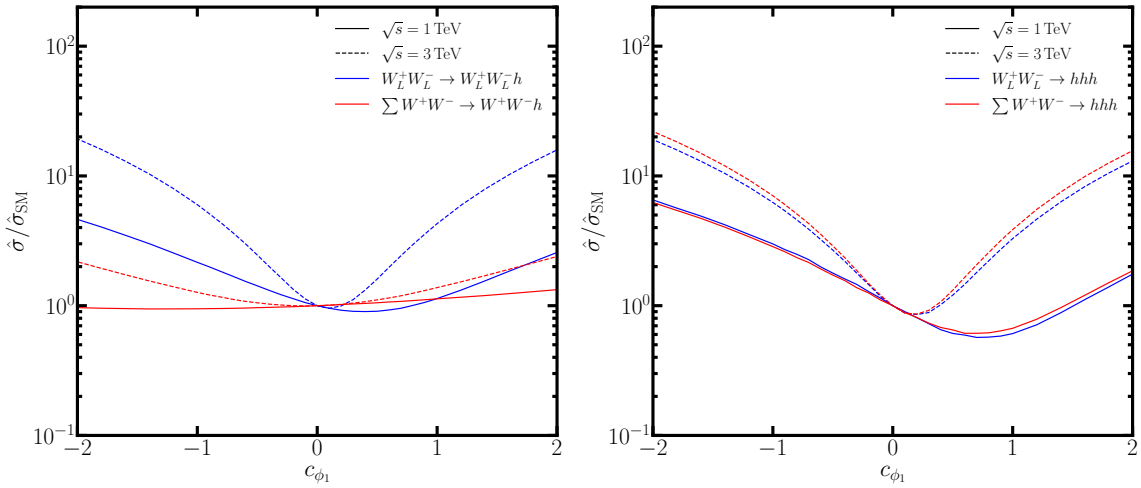

Figure 7. $\hat{\sigma}/\hat{\sigma}_{\mathrm{SM}}$ for $W^+W^- \to W^+W^- h$ and $W^+W^- \to hhh$ as functions of c_{Φ_1}.

higher energy which is mainly due to the logarithm enhancement of the SM cross section as discussed in previous section.

Similar results for c_{Φ_1} are shown in figure 6 and figure 7. Again, $WW \to WWh$ is dominated by transverse polarizations. Compared with the dependence on c_6, the cross section is much more enhanced by c_{Φ_1} due to the momentum dependence of $\mathcal{O}_{\Phi_1}$ operator. Further, this momentum dependence of $\mathcal{O}_{\Phi_1}$ also overcomes the logarithms in SM cross section, thus higher energy corresponds to higher sensitivities. Finally, we comment that the shapes of cross sections vs. $c_6(c_{\Phi_1})$ are parabolic. This is consistent with the fact that only terms up to the order of $\frac{1}{\Lambda^2}$ are kept in the amplitude level. As a result, the cross sections are quadratic functions of $c_6(c_{\Phi_1})$.

In this section, we discussed the cross section for $2 \to 3$ VBS processes and their dependence on c_6 and c_{Φ_1} which provides the basic ideas about the sources of the sensitivities.

JHEP10(2021)099

In the next section, we will proceed to discuss the measurement of c_6 and c_{Φ_1} with more realistic setup at both hadron and lepton colliders.

4 VBS processes at hadron/lepton collider

4.1 Signal processes

In section 3, we analyzed VBS processes with three bosons in the final state at high energy, taking $W_L^+W_L^- \to W_L^+W_L^-h$ and $W_L^+W_L^- \to hhh$ as two examples. We found that they are sensitive to dim-6 operators in the SMEFT as shown in figure 5 and figure 7. In this section we continue to analyze the corresponding full processes at hadron and lepton colliders using `MadGraph` [66] with the SMEFT model file from ref. [72].

Since the aim of this paper is to illustrate important and crucial behaviors of $2 \to 3$ VBS processes, we don't plan to cover all related processes here. Instead, we choose the following processes as benchmarks:

$$l^+l^- \to \nu_l\bar{\nu}_l W_L^+W_L^-h \qquad l^+l^- \to \nu_l\bar{\nu}_l hhh \tag{4.1}$$

$$pp \to jjW_L^\pm W_L^\pm h \qquad pp \to jjhhh \tag{4.2}$$

where l is either μ or e. Processes in eq. (4.1) can be explored at a series of future lepton colliders, including CLIC [29–31] ($1\text{TeV} < \sqrt{s} < 3\text{TeV}$) and the recently proposed muon colliders [32–36] ($3\text{TeV} < \sqrt{s} < 30\text{TeV}$). Processes in eq. (4.2) can be explored at the HL-LHC, HE-LHC [14] and the future 100 TeV pp colliders [37, 73]. Notice that we focus on the same-sign Ws for $pp \to jjW_LW_Lh$ due to the suppressions of relevant SM backgrounds for this process compared with the opposite-sign one. We will devote a comprehensive survey of all relevant VBS processes in future works.

4.2 Signal cross sections

In this section, we will examine the cross section for relevant signal processes listed in last section, especially the dependence of the cross section on c_6 and c_{Φ_1} and the comparison with SM cross section. In the following, we will present the results for WWh and hhh productions respectively.

Production of WWh. In this category, we considered following processes for hadron and lepton colliders:

$$p\,p \to jjW^\pm W^\pm h, \tag{4.3}$$

$$l^+\,l^- \to \nu_l\bar{\nu}_l W^+W^-h, \tag{4.4}$$

where, as stated in last section, we choose same-sign W-pair for hadron collider to suppress the backgrounds.

The cross sections for $\mu^+\mu^- \to \nu_\mu\bar{\nu}_\mu W_L^+W_L^-h$ for different choices of c_6 and c_{Φ_1} are listed in table 1 and table 2 respectively. The cuts we imposed on the cross section calculation are listed in table 3. Note that we impose a slightly stronger cuts for the case in table 1 (as well as the case in table 4 below). As in this case, the enhancement due to c_6

JHEP10(2021)099

Cross sections (pb) for $\mu^+\mu^- \to \nu_\mu\bar{\nu}_\mu W_L^+ W_L^- h$ with $c_{\Phi_1} = 0$					
c_6	-2	-1	0	1	2
1 TeV	4.17×10^{-9}	1.57×10^{-9}	8.22×10^{-10}	1.93×10^{-9}	4.90×10^{-9}
3 TeV	1.79×10^{-6}	6.98×10^{-7}	3.71×10^{-7}	8.01×10^{-7}	2.00×10^{-6}
5 TeV	6.10×10^{-6}	2.43×10^{-6}	1.32×10^{-6}	2.74×10^{-6}	6.72×10^{-6}
10 TeV	1.94×10^{-5}	7.98×10^{-6}	4.38×10^{-6}	8.74×10^{-6}	2.09×10^{-5}
14 TeV	2.99×10^{-5}	1.25×10^{-5}	7.11×10^{-6}	1.36×10^{-5}	3.22×10^{-5}
30 TeV	6.45×10^{-5}	2.82×10^{-5}	1.58×10^{-5}	2.95×10^{-5}	6.68×10^{-5}

Table 1. The cross section for $\mu^+\mu^- \to \nu_\mu\bar{\nu}_\mu W_L^+ W_L^- h$ with $c_{\Phi_1} = 0$ at different c.m. energies. Five benchmark points of c_6 are displayed in different columns. The cuts $m_{\nu\nu} > 150\,\text{GeV}$, $p_T(W,h) > 150\,\text{GeV}$ are implemented to obtain these cross sections.

Cross sections (pb) for $\mu^+\mu^- \to \nu_\mu\bar{\nu}_\mu W_L^+ W_L^- h$ with $c_6 = 0$					
c_{Φ_1}	-2	-1	0	1	2
1 TeV	6.23×10^{-7}	6.70×10^{-7}	7.69×10^{-7}	9.27×10^{-7}	1.14×10^{-6}
3 TeV	2.65×10^{-5}	2.34×10^{-5}	2.47×10^{-5}	2.96×10^{-5}	3.95×10^{-5}
5 TeV	8.85×10^{-5}	6.71×10^{-5}	6.43×10^{-5}	8.13×10^{-5}	1.17×10^{-4}
10 TeV	4.09×10^{-4}	2.22×10^{-4}	1.71×10^{-4}	2.61×10^{-4}	4.72×10^{-4}
14 TeV	8.63×10^{-4}	3.95×10^{-4}	2.56×10^{-4}	4.38×10^{-4}	9.39×10^{-4}
30 TeV	4.97×10^{-3}	1.60×10^{-3}	5.07×10^{-4}	1.66×10^{-3}	5.04×10^{-3}

Table 2. The same as table 1, but for $c_6 = 0$ with five benchmark points of c_{Φ_1} at different c.m. energies. The cuts $m_{\nu\nu} > 150\,\text{GeV}$ is implemented to obtain these cross sections.

	WWh		hhh	
Beams:	$\mu^+\mu^-$	pp	$\mu^+\mu^-$	pp
Varying c_6:	$m_{\nu\nu} > 150\,\text{GeV}$ $p_T(W,h) > 150\,\text{GeV}$	$m_{j_1j_2} > 150\,\text{GeV}$ $p_T(W,h) > 150\,\text{GeV}$ $\eta_{j_1} \times \eta_{j_2} < 0$ $\lvert\Delta\eta_{j_1j_2}\rvert > 2.5$	$m_{\nu\nu} > 150\,\text{GeV}$	$m_{j_1j_2} > 150\,\text{GeV}$ $\eta_{j_1} \times \eta_{j_2} < 0$ $\lvert\Delta\eta_{j_1j_2}\rvert > 2.5$
Varying c_{Φ_1}:	$m_{\nu\nu} > 150\,\text{GeV}$	$m_{j_1j_2} > 150\,\text{GeV}$ $\eta_{j_1} \times \eta_{j_2} < 0$ $\lvert\Delta\eta_{j_1j_2}\rvert > 2.5$	$m_{\nu\nu} > 150\,\text{GeV}$	$m_{j_1j_2} > 150\,\text{GeV}$ $\eta_{j_1} \times \eta_{j_2} < 0$ $\lvert\Delta\eta_{j_1j_2}\rvert > 2.5$

Table 3. The cuts used for processes with WWh and hhh final states at pp and lepton colliders respectively.

JHEP10(2021)099

Cross sections (pb) for $pp \to jjW_L^\pm W_L^\pm h$ with $c_{\Phi_1} = 0$					
c_6	-2	-1	0	1	2
14 TeV	6.35×10^{-7}	2.81×10^{-7}	1.68×10^{-7}	3.01×10^{-7}	6.79×10^{-7}
27 TeV	3.58×10^{-6}	1.68×10^{-6}	1.09×10^{-6}	1.78×10^{-6}	3.76×10^{-6}
100 TeV	3.28×10^{-5}	1.82×10^{-5}	1.38×10^{-5}	1.87×10^{-5}	3.34×10^{-5}

Table 4. The cross section for $pp \to jjW_L^\pm W_L^\pm h$ with $c_{\Phi_1} = 0$ at different c.m. energies. Five benchmark points of c_6 are displayed in different columns. The cuts $m_{jj} > 150\,\text{GeV}$, $p_T(W, h) > 150\,\text{GeV}$ as well as the VBS selections ($\eta_{j_1} \times \eta_{j_2} < 0$ and $|\Delta\eta_{j_1 j_2}| > 2.5$) are implemented to obtain these cross sections.

Cross sections (pb) for $pp \to jjW_L^\pm W_L^\pm h$ with $c_6 = 0$					
c_{Φ_1}	-2	-1	0	1	2
14 TeV	2.58×10^{-5}	2.65×10^{-5}	2.88×10^{-5}	3.29×10^{-5}	3.90×10^{-5}
27 TeV	1.27×10^{-4}	1.20×10^{-4}	1.27×10^{-4}	1.49×10^{-4}	1.83×10^{-4}
100 TeV	1.26×10^{-3}	9.91×10^{-4}	9.70×10^{-4}	1.23×10^{-3}	1.72×10^{-3}

Table 5. The same as table 4, but for $c_6 = 0$ with five benchmark points of c_{Φ_1} at different c.m. energies. The cuts $m_{jj} > 150\,\text{GeV}$ and the VBS selections ($\eta_{j_1} \times \eta_{j_2} < 0$ and $|\Delta\eta_{j_1 j_2}| > 2.5$) are implemented to obtain these cross sections.

is not large which is overwhelmed by the Sudakov logarithms from soft/collinear behavior in the SM cross section. We thus impose additional p_T cuts on final states to avoid such soft/collinear regions.

From these tables, we find that the behavior of the cross section with respect to c_6 and c_{Φ_1} is similar to what we observed in section 3. For WWh final state, the dependence of the cross section on c_6 will be slightly weaker at higher energy, i.e. $\frac{\sigma(c_6=2)}{\sigma_{\text{SM}}} = 5.96(4.23)$ for $\sqrt{s} = 1(30)\,\text{TeV}$. On the other hand, the cross section enhancement due to c_{Φ_1} will be stronger at higher energy, i.e. $\frac{\sigma(c_{\Phi_1}=2)}{\sigma_{\text{SM}}} = 1.48(9.94)$ for $\sqrt{s} = 1(30)\,\text{TeV}$. Hence, by just measuring the total events, we will have stronger constraints on c_{Φ_1} than c_6 with a 14 TeV or even 30 TeV muon collider machine.

In the simulation we have chosen longitudinal polarizations for W bosons in the final states. The reason is that the cross sections for summing over the polarizations of the final state $W^\pm$s are dominated by transverse polarizations, whereas deviation of Higgs self-couplings mainly modifies cross sections of all longitudinal vector bosons only. So in order to study the influence from high dimension operators, in practice, the longitudinal polarizations should be picked using some technics [67–71]. Detailed comparison between cross sections summing over polarizations of W bosons in the final states and the ones with longitudinal W bosons in the final states can be found in section A.

The cross section for $pp \to jjW_L^\pm W_L^\pm h$ with different choices of c_6 and c_{Φ_1} are listed in table 4 and table 5. The relevant cuts applied on this process are also listed in table 3. The

JHEP10(2021)099

Cross sections (pb) for $\mu^+\mu^- \to \nu_\mu\bar{\nu}_\mu hhh$ with $c_{\Phi_1} = 0$					
c_6	-2	-1	0	1	2
1 TeV	4.42×10^{-8}	1.06×10^{-8}	3.39×10^{-9}	2.25×10^{-8}	6.76×10^{-8}
3 TeV	1.93×10^{-6}	5.66×10^{-7}	2.78×10^{-7}	1.08×10^{-6}	2.94×10^{-6}
5 TeV	4.91×10^{-6}	1.57×10^{-6}	9.50×10^{-7}	3.03×10^{-6}	7.74×10^{-6}
10 TeV	1.25×10^{-5}	4.59×10^{-6}	3.46×10^{-6}	8.75×10^{-6}	1.95×10^{-5}
14 TeV	1.80×10^{-5}	6.70×10^{-6}	5.38×10^{-6}	1.30×10^{-5}	2.88×10^{-5}
30 TeV	3.50×10^{-5}	1.77×10^{-5}	1.41×10^{-5}	2.92×10^{-5}	5.42×10^{-5}

Table 6. The cross section for $\mu^+\mu^- \to \nu_\mu\bar{\nu}_\mu hhh$ with $c_{\Phi_1} = 0$ at different c.m. energies. Five benchmark points of c_6 are displayed in different columns. The cut $m_{\nu\nu} > 150\,\text{GeV}$ is implemented to obtain these cross sections.

Cross sections (pb) for $\mu^+\mu^- \to \nu_\mu\bar{\nu}_\mu hhh$ with $c_6 = 0$					
c_{Φ_1}	-2	-1	0	1	2
1 TeV	2.78×10^{-8}	1.08×10^{-8}	3.39×10^{-9}	5.56×10^{-9}	1.73×10^{-8}
3 TeV	3.01×10^{-6}	1.11×10^{-6}	2.78×10^{-7}	5.43×10^{-7}	1.89×10^{-6}
5 TeV	1.33×10^{-5}	4.47×10^{-6}	9.50×10^{-7}	2.38×10^{-6}	8.76×10^{-6}
10 TeV	7.83×10^{-5}	2.38×10^{-5}	3.46×10^{-6}	1.50×10^{-5}	5.97×10^{-5}
14 TeV	1.77×10^{-4}	4.97×10^{-5}	5.38×10^{-6}	3.73×10^{-5}	1.44×10^{-4}
30 TeV	1.07×10^{-3}	2.77×10^{-4}	1.41×10^{-5}	2.44×10^{-4}	9.86×10^{-4}

Table 7. The same as table 6, but for $c_6 = 0$ with five benchmark points of c_{Φ_1} at different c.m. energies.

overall behavior of the cross section with respect to c_6 and c_{Φ_1} is similar to the case at muon collider, however, the sensitivity is weaker: $\frac{\sigma(c_6=2)}{\sigma_{\text{SM}}} = 4.04(2.42)$ and $\frac{\sigma(c_{\Phi_1}=2)}{\sigma_{\text{SM}}} \approx 1.35(1.77)$ for $\sqrt{s} = 14(100)\,\text{TeV}$.

Production of *hhh*. In this category, the processes we considered at hadron and lepton colliders are:

$$pp \to jjhhh, \tag{4.5}$$

$$l^+l^- \to \nu_l\bar{\nu}_l hhh. \tag{4.6}$$

The cross section for $\mu^+\mu^- \to \nu_\mu\bar{\nu}_\mu hhh$ for different choices of c_6 and c_{Φ_1} are listed in table 6 and table 7. The cuts we imposed on the process are also listed in table 3. The cross sections for hhh production are slightly smaller than that of WWh production, while the sensitivity on c_{Φ_1} from hhh channel is much stronger than that in WWh channel as we can see from table 7, $\frac{\sigma(c_{\Phi_1}=2)}{\sigma_{\text{SM}}} \approx 70$ at $\sqrt{s} = 30\,\text{TeV}$. However, the enhancement due to c_6 is moderate: $\frac{\sigma(c_6=2)}{\sigma_{\text{SM}}} \approx 4$ at $\sqrt{s} = 30\,\text{TeV}$. The cross section and its dependence on c_6 and

JHEP10(2021)099

Cross sections (pb) for $pp \to jjhhh$ with $c_{\Phi_1} = 0$					
c_6	-2	-1	0	1	2
14 TeV	1.99×10^{-6}	5.77×10^{-7}	2.97×10^{-7}	1.16×10^{-6}	3.12×10^{-6}
27 TeV	9.46×10^{-6}	2.93×10^{-6}	1.50×10^{-6}	5.48×10^{-6}	1.45×10^{-5}
100 TeV	7.91×10^{-5}	2.65×10^{-5}	1.48×10^{-5}	4.30×10^{-5}	1.13×10^{-4}

Table 8. The cross section for $pp \to jjhhh$ with $c_{\Phi_1} = 0$ at different c.m. energies. Five benchmark points of c_6 are displayed in different columns. The cut $m_{j_1 j_2} > 150\,\text{GeV}$ and VBS selections ($\eta_{j_1} \times \eta_{j_2} < 0$ and $|\Delta\eta_{j_1 j_2}| > 2.5$) are implemented to obtain these cross sections.

Cross sections (pb) for $pp \to jjhhh$ with $c_6 = 0$					
c_{Φ_1}	-2	-1	0	1	2
14 TeV	2.94×10^{-6}	1.10×10^{-6}	2.97×10^{-7}	5.33×10^{-7}	1.83×10^{-6}
27 TeV	1.97×10^{-5}	6.99×10^{-6}	1.50×10^{-6}	3.75×10^{-6}	1.35×10^{-5}
100 TeV	3.31×10^{-4}	1.02×10^{-4}	1.48×10^{-5}	7.04×10^{-5}	2.69×10^{-4}

Table 9. The same as table 8, but for $c_6 = 0$ with five benchmark points of c_{Φ_1} at different c.m. energies.

c_{Φ_1} for $pp \to jjhhh$ are listed in table 8 and table 9. Similar to muon collider case, the sensitivities on both c_6 and c_{Φ_1} are stronger from hhh production than that from WWh production. At $\sqrt{s} = 100\,\text{TeV}$, we have $\frac{\sigma(c_6=2)}{\sigma_{\text{SM}}} \approx 8$ and $\frac{\sigma(c_{\Phi_1})}{\sigma_{\text{SM}}} \approx 18$.

4.3 Results and prospects

Based on the cross section results in section 4.2, in figure 8 and figure 9, we show the cross section as function of the c.m. energies for both WWh and hhh productions where the black curve is for the SM case and different colors (solid or dashed) are for the cases either c_6 or c_{Φ_1} is non-zero. Notice that the cross section increases logarithmically as the main production mechanism is VBS. All these processes provide some sensitivities on both c_6 and c_{Φ_1} as can be seen by comparing the colored curves with the SM one.

In figure 10 and figure 11, we show the cross section difference induced by $\mathcal{O}_6$ and $\mathcal{O}_{\Phi_1}$ compared with the SM one for WWh and hhh production respectively. In general, the sensitivity at lepton collider will be stronger than that at hadron collider. Further, the sensitivity on c_6 ($\mathcal{O}_6$) decreases as energy increases, as we have indicated in previous sections, due to the logarithmical enhancement of the SM cross section. On the other hand, the sensitivity on c_{Φ_1} ($\mathcal{O}_{\Phi_1}$) increases at high energy due to the momentum dependence in the $\mathcal{O}_{\Phi_1}$ operator.

Based on the deviation in the cross section due to $\mathcal{O}_6$ and $\mathcal{O}_{\Phi_1}$ operators contributions, we can estimate the allowed region of c_6 and c_{Φ_1} under some simplified assumptions. First,

JHEP10(2021)099

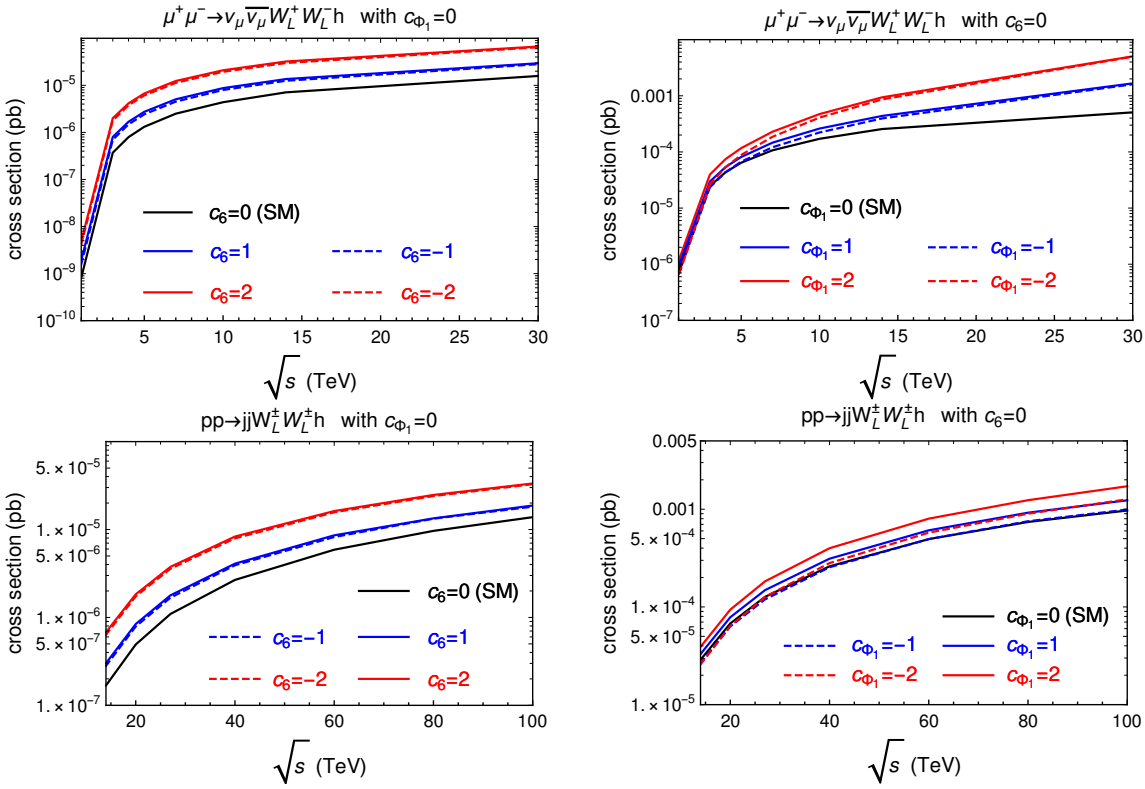

Figure 8. The cross section for WWh production at muon collider (upper panels) and hadron collider (lower panels) as function of $\sqrt{s}$.

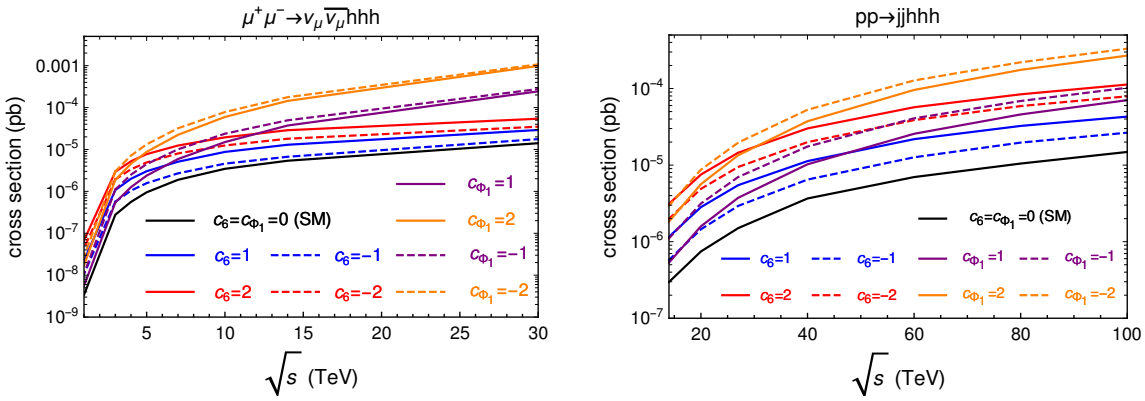

Figure 9. The vary of cross sections for $c_6 = \pm 1, \pm 2$ with $c_{\Phi_1} = 0$ and $c_{\Phi_1} = \pm 1, \pm 2$ with $c_6 = 0$ for $\mu^+\mu^- \to \nu_\mu \overline{\nu}_\mu hhh$ from $\sqrt{s} = 1$ to 30 TeV (left panel) and $pp \to jjhhh$ from $\sqrt{s} = 14$ to 100 TeV (right panel).

the full signal to background analysis is beyond our scope.[3] In our analysis, we simply

[3]However, we'd like to comment that the background at lepton collider can be well controlled, as the cut on invariant mass of all final states can help to remove most of the background due to the VBS nature of our signal process. While at hadron collider, we have chosen same-sign W boson production, as the specific 2 same-sign lepton signals will also suppress the possible background at hadron collider.

JHEP10(2021)099

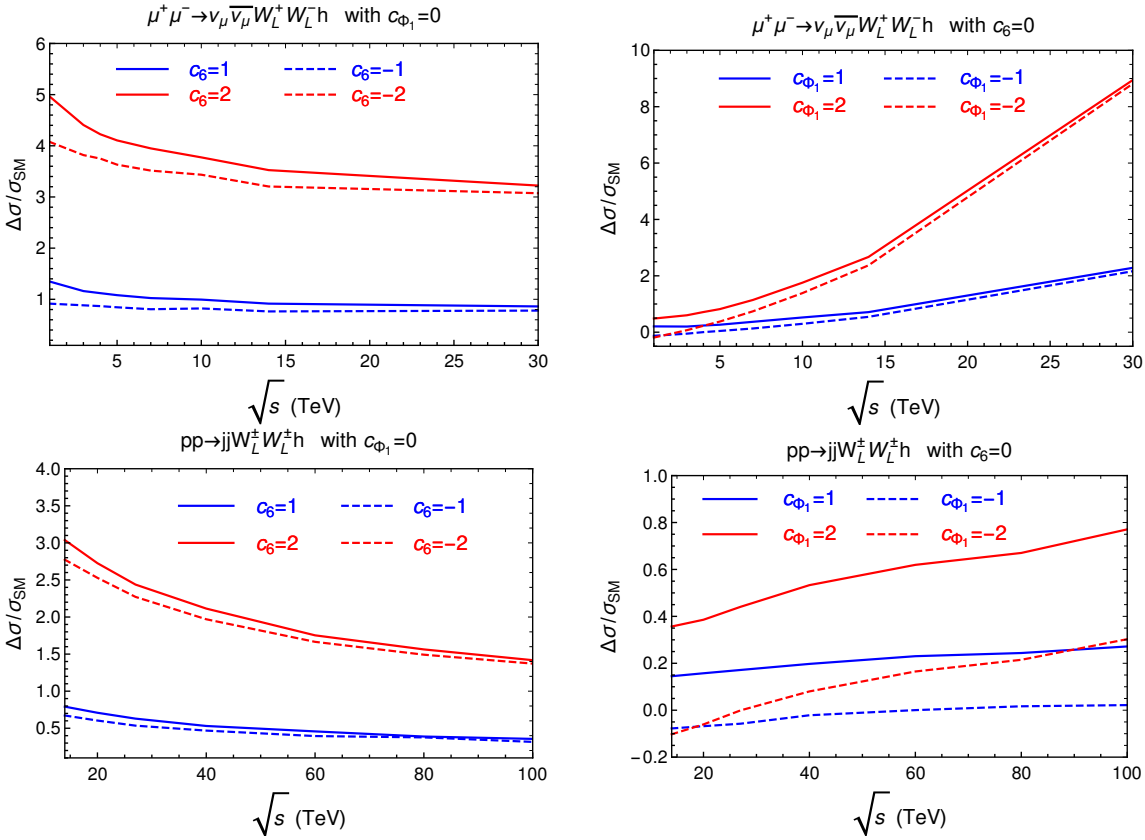

Figure 10. The $\Delta\sigma/\sigma_{SM}$ for $c_6 = \pm 1, \pm 2$ with $c_{\Phi_1} = 0$ and $c_{\Phi_1} = \pm 1, \pm 2$ with $c_6 = 0$ for $\mu^+\mu^- \to \nu_\mu \overline{\nu}_\mu WWh$ from $\sqrt{s} = 1$ to 30 TeV (upper panel) and $pp \to jjWWh$ from $\sqrt{s} = 14$ to 100 TeV (lower panel) where $\Delta\sigma \equiv \sigma_{\rm tot} - \sigma_{SM}$.

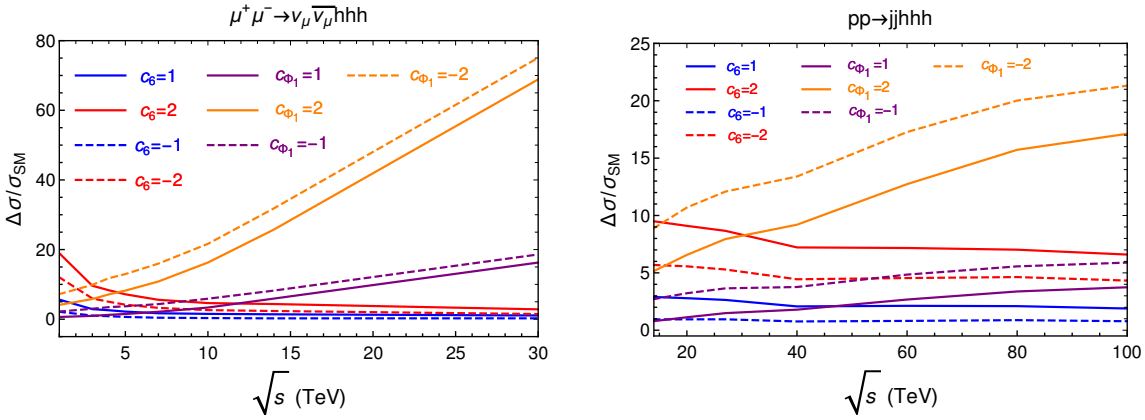

Figure 11. The $\Delta\sigma/\sigma_{SM}$ for $c_6 = \pm 1, \pm 2$ with $c_{\Phi_1} = 0$ and $c_{\Phi_1} = \pm 1, \pm 2$ with $c_6 = 0$ for $\mu^+\mu^- \to \nu_\mu \overline{\nu}_\mu hhh$ from $\sqrt{s} = 1$ to 30 TeV (left panel) and $pp \to jjhhh$ from $\sqrt{s} = 14$ to 100 TeV (right panel) where $\Delta\sigma \equiv \sigma_{\rm tot} - \sigma_{SM}$.

JHEP10(2021)099

Allowed region from the $\mu^+\mu^- \to \nu_\mu \bar{\nu}_\mu W_L^+ W_L^- h$ process					
$\sqrt{s}$ (TeV)	$\mathcal{L}$ (ab^{-1})	c_6 ($c_{\Phi_1} = 0$) x-sec only		c_{Φ_1} ($c_6 = 0$) x-sec only	
		1σ	2σ	1σ	2σ
1	1.2	–	–	–	–
3	4.4	–	–	$[-2.54, 0.71]$	$[-3.07, 1.18]$
5	12	$[-0.65, 0.53]$	$[-0.89, 0.77]$	$[-1.02, 0.30]$	$[-1.22, 0.50]$
10	20	$[-0.44, 0.35]$	$[-0.60, 0.51]$	$[-0.43, 0.13]$	$[-0.50, 0.22]$
14	33	$[-0.37, 0.28]$	$[-0.50, 0.41]$	$[-0.23, 0.10]$	$[-0.29, 0.15]$
30	100	$[-0.23, 0.18]$	$[-0.31, 0.26]$	$[-0.07, 0.04]$	$[-0.09, 0.06]$

Table 10. The range of c_6 with $c_{\Phi_1} = 0$ and c_{Φ_1} with $c_6 = 0$ for $\mu^+\mu^- \to \nu_\mu \bar{\nu}_\mu W_L^+ W_L^- h$ process at lepton colliders with various benchmarks $\sqrt{s}$ and $\mathcal{L}$. The 1σ and 2σ allowed regions on c_6 and c_{Φ_1} are calculated from the definition in eq. (4.7) which only rely on the size of cross sections. The notation "$-$" means either $N_{\rm SM} < 1$ or $|N_{\rm BSM} - N_{\rm SM}| < 1$.

Allowed region from the $\mu^+\mu^- \to \nu_\mu \bar{\nu}_\mu hhh$ process					
$\sqrt{s}$ (TeV)	$\mathcal{L}$ (ab^{-1})	c_6 ($c_{\Phi_1} = 0$) x-sec only		c_{Φ_1} ($c_6 = 0$) x-sec only	
		1σ	2σ	1σ	2σ
1	1.2	–	–	–	–
3	4.4	–	–	–	–
5	12	$[-1.00, 0.46]$	$[-1.27, 0.73]$	$[-0.34, 0.76]$	$[-0.54, 0.96]$
10	20	$[-0.95, 0.30]$	$[-1.14, 0.50]$	$[-0.14, 0.41]$	$[-0.23, 0.50]$
14	33	$[-0.93, 0.21]$	$[-1.08, 0.37]$	$[-0.10, 0.24]$	$[-0.16, 0.30]$
30	100	$[-0.75, 0.12]$	$[-0.84, 0.21]$	$[-0.04, 0.10]$	$[-0.06, 0.12]$

Table 11. The same as table 10 but for $\mu^+\mu^- \to \nu_\mu \bar{\nu}_\mu hhh$ process at lepton colliders.

follow the strategy used in ref. [50] to count the deviation of signal events from SM ones. Further, we define the significance of non-SM events over SM ones as:

$$\text{significance} \sim \frac{|N_{\rm BSM} - N_{\rm SM}|}{\sqrt{N_{\rm SM}}}. \tag{4.7}$$

where $N_{\rm SM}$ and $N_{\rm BSM}$ are the event number of SM processes and the case with $\mathcal{O}_6$ or $\mathcal{O}_{\Phi_1}$ operator respectively. For $\mu^+\mu^- \to \nu_\mu \bar{\nu}_\mu W_L^+ W_L^- h$ process, $N_i \equiv \sigma_i(\mu^+\mu^- \to \nu_\mu \bar{\nu}_\mu W_L^+ W_L^- h) \times \left[\text{BR}(h \to b\bar{b})\right] \times [\text{BR}(W^\pm \to \text{all})]^2 \times \mathcal{L}$ where $\mathcal{L}$ is the integrated luminosity. Here we assume that all of leptonic, semileptonic and hadronic decay modes from opposite sign W boson pair can be detected at future muon collider experiments. For $pp \to jjW_L^\pm W_L^\pm h$ process, $N_i \equiv \sigma_i(pp \to jjW_L^\pm W_L^\pm h) \times \left[\text{BR}(h \to b\bar{b})\right] \times [\text{BR}(W^\pm \to l^\pm \nu)]^2 \times \mathcal{L}$, where we only focus on the leptonic decay modes of same sign W boson pair at hadron colliders to avoid possible huge SM backgrounds. For the hhh processes, $N_i \equiv \sigma_i \times$

JHEP10(2021)099

Allowed region from the $pp \to jjW_L^\pm W_L^\pm h$ process					
$\sqrt{s}$ (TeV)	$\mathcal{L}$ (ab^{-1})	c_6 ($c_{\Phi_1} = 0$) x-sec only		c_{Φ_1} ($c_6 = 0$) x-sec only	
		1σ	2σ	1σ	2σ
14	3	–	–	$[-8.04, 3.02]$	$[-11.34, 4.62]$
27	15	–	–	$[-2.76, 0.87]$	$[-3.29, 1.46]$
100	30	$[-0.99, 0.92]$	$[-1.38, 1.32]$	$[-1.08, 0.23]$	$[-1.24, 0.40]$

Table 12. The same as table 10 but for $pp \to jjW_L^\pm W_L^\pm h$ process at hadron colliders.

Allowed region from the $pp \to jjhhh$ process					
$\sqrt{s}$ (TeV)	$\mathcal{L}$ (ab^{-1})	c_6 ($c_{\Phi_1} = 0$) x-sec only		c_{Φ_1} ($c_6 = 0$) x-sec only	
		1σ	2σ	1σ	2σ
14	3	–	–	–	–
27	15	$[-0.80, 0.33]$	$[-1.00, 0.53]$	$[-0.19, 0.79]$	$[-0.33, 0.90]$
100	30	$[-0.55, 0.14]$	$[-0.65, 0.24]$	$[-0.07, 0.30]$	$[-0.13, 0.35]$

Table 13. The same as table 10 but for $pp \to jjhhh$ process at hadron colliders.

$\left[\text{BR}(h \to b\bar{b})\right]^3 \times \mathcal{L}$ where σ_i is the production cross section for $\mu^+\mu^- \to \nu_\mu \bar{\nu}_\mu hhh$ or $pp \to jjhhh$ process at muon colliders or pp colliders. We also require both $N_{\text{SM}} > 1$ and $|N_{\text{BSM}} - N_{\text{SM}}| > 1$ in our analysis. The allowed region for c_6 and c_{Φ_1} at 1- and 2-σ level are summarized in table 10–13. Note that several entries of the allowed regions for c_{Φ_1} are beyond $[-2, 2]$, which should be treated with caution. As in our analysis, we only calculate the cross section within $[-2, 2]$ for both c_6 and c_{Φ_1}, the interpolation is only valid within this region.

The allowed regions for c_6 (red) and c_{Φ_1} (blue) are also shown in figure 12 where darker color indicates the 1-σ region, while lighter one indicates the 2-σ region. We also denote those channels that cannot provide enough event rate as hatched region. It is clear from this plot that, in general, high energy muon collider is more powerful than HE-LHC in constraining c_6 and c_{Φ_1}. Furthermore, both WWh and hhh production are more sensitive to c_{Φ_1} than c_6. However, for both c_6 and c_{Φ_1}, we will have higher sensitivities with higher energy at both lepton and hadron colliders thanks to the increase of cross sections.

We further study the allowed parameter space on the (c_6, c_{Φ_1}) plane for 30 TeV muon collider with $\mathcal{L} = 100$ ab^{-1} and 100 TeV hadron collider with $\mathcal{L} = 30$ ab^{-1} in figure 13. First, the dashed (solid) lines represent 1-σ (2-σ) allowed regions. Then, we include four channels with $\mu^+\mu^- \to \nu_\mu \overline{\nu_\mu} W_L^+ W_L^- h$ (black), $\mu^+\mu^- \to \nu_\mu \overline{\nu_\mu} hhh$ (blue), $pp \to jjW_L^\pm W_L^\pm h$ (purple), and $pp \to jjhhh$ (red). For comparison purpose, we uniformly apply the stronger cuts in table 3 for both $\mu^+\mu^- \to \nu_\mu \overline{\nu_\mu} W_L^+ W_L^- h$ and $pp \to jjW_L^\pm W_L^\pm h$. We can find the most stringent constraint on the (c_6, c_{Φ_1}) plane comes from the process $\mu^+\mu^- \to \nu_\mu \overline{\nu_\mu} W_L^+ W_L^- h$. However, $\mu^+\mu^- \to \nu_\mu \overline{\nu_\mu} hhh$ and $pp \to jjhhh$ processes can still help us to cover some parameter space on the (c_6, c_{Φ_1}) plane which the process $\mu^+\mu^- \to \nu_\mu \overline{\nu_\mu} W_L^+ W_L^- h$ cannot reach.

JHEP10(2021)099

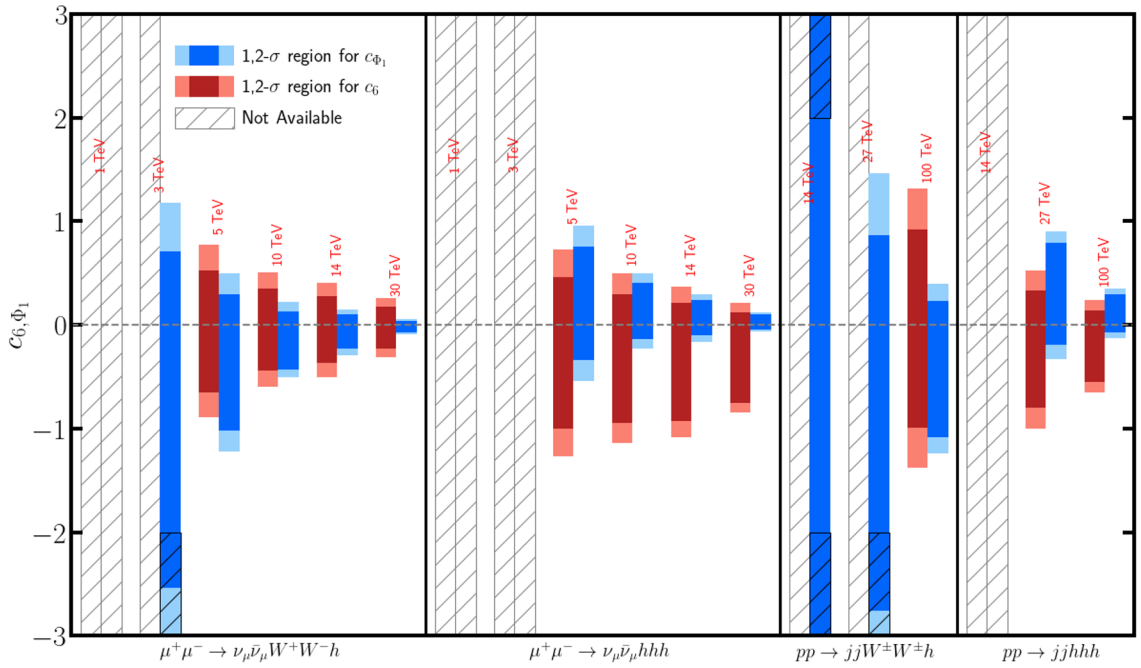

Figure 12. The allowed region for c_6 (red) and c_{Φ_1} (blue) from different channels. The darker color indicates the 1-σ region, while lighter one indicates the 2-σ region. The hatched region are not available either due to low event rate or beyond $[-2, 2]$.

$2 \to 3$ VBS processes are not the only channels to study the measurement of Higgs self-couplings at colliders. At the LHC, and future hadron colliders, di-Higgs production through gluon fusion remains the dominant channel [8–15]. Whereas at future lepton colliders, di-Higgs production through $2 \to 2$ VBS, i.e. $VV \to hh$, become dominant [30, 31, 34–36]. In terms of Wilson coefficients, both c_6 and c_{Φ_1} can also be measured with either $gg \to hh$ or $VV \to hh$. Furthermore, c_{Φ_1} can be measured with $2 \to 1$ vector boson fusion, $2 \to 2$ VBS with gauge boson final states and etc. See also [7] and [74] for overall reviews.

A comparison between muon colliders and other future colliders was done in [35], showing clear advantages of muon colliders. Here we mainly compare our results with $VV \to hh$ at muon colliders. In ref. [35], the projective limits on c_6 and c_{Φ_1} at muon colliders with $\sqrt{s} = 14\,\text{TeV}$ and the integrated luminosity of 20 ab^{-1} are obtained by combining $VV \to hh$ and $VV \to hhh$. The results are

$$c_6 \in [-0.66, 0.23], \qquad c_{\Phi_1} \in [-0.17, 0.30] \tag{4.8}$$

at 95% for $\Lambda = 1\,\text{TeV}$. This is close to our similar results for both $VV \to W_L^+ W_L^- h$ and $VV \to hhh$, as can be seen in table 10 and table 11, indicating that constraints on Higgs self-couplings from $2 \to 3$ VBS might be comparable to $VV \to hh$ at muon colliders. Of course, more careful and in-depth studies are obviously needed.

JHEP10(2021)099

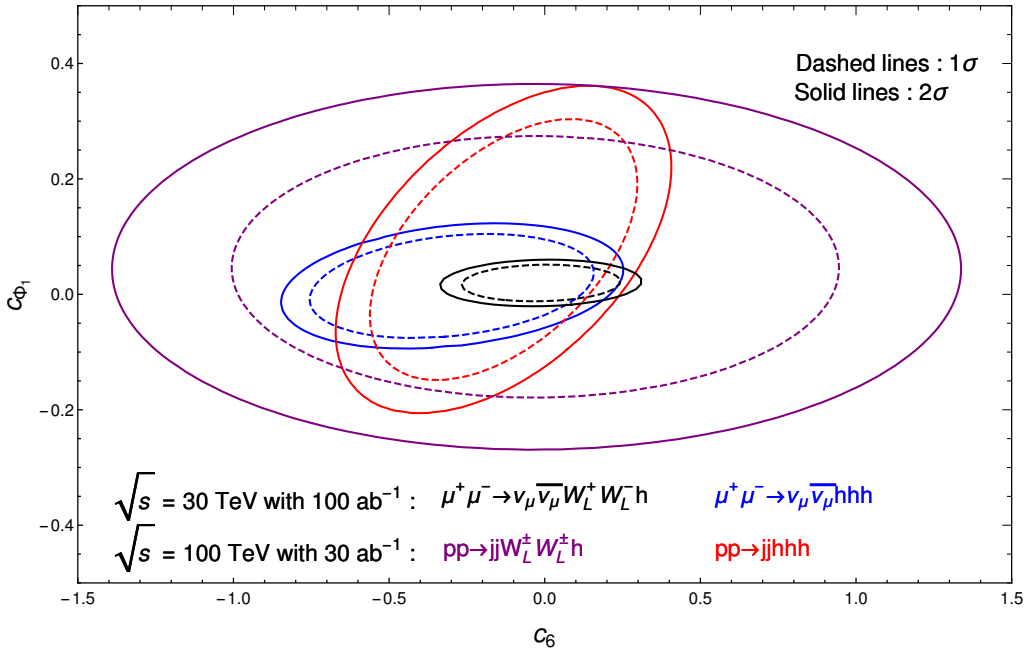

Figure 13. The allowed parameter space on the (c_6, c_{Φ_1}) plane for 30 TeV muon collider with $\mathcal{L} = 100$ ab^{-1} and 100 TeV hadron collider with $\mathcal{L} = 30$ ab^{-1}. The dashed (solid) lines represent 1-σ (2-σ) allowed regions and four channels are labelled with $\mu^+\mu^- \to \nu_\mu\overline{\nu_\mu}W_L^+W_L^-h$ (black), $\mu^+\mu^- \to \nu_\mu\overline{\nu_\mu}hhh$ (blue), $pp \to jjW_L^\pm W_L^\pm h$ (purple), and $pp \to jjhhh$ (red).

5 Conclusions

Measuring Higgs self-couplings is a crucial task for the future collider experiments. It will uncover the nature of the discovered SM-like Higgs bosn, the origin of EWSB, and the shape of the Higgs potential, etc. In this work, we studied the $2 \to 3$ VBS processes under the framework of SMEFT, using $W_L^\pm W_L^\pm \to W_L^\pm W_L^\pm h$ and $W_L^+W_L^- \to hhh$ as examples.

First, the behavior of the amplitudes for those processes at high energy is analysed using GET. We found that compared with SM contributions, the BSM contribution will be enhanced at high energy as $\frac{\mathcal{A}_{\rm BSM}}{\mathcal{A}_{\rm SM}} \sim \frac{E^2}{\Lambda^2}$. Physically, this behavior comes from the combination of the following two factors: SM amplitudes are suppressed by the energy in the propagators; BSM amplitudes can stay constant due to contact vertex from $\mathcal{O}_6$ or increase with energy due to the momentum dependence in $\mathcal{O}_{\Phi_1}$. By numerically calculating the cross section for these $2 \to 3$ processes, we showed the sensitivities of these processes to c_6 and c_{Φ_1} in figure 4 to figure 7.

Second, the processes $pp \to jjW_L^\pm W_L^\pm h$ and $pp \to jjhhh$ at pp colliders and $\mu^+\mu^- \to \nu_\mu\overline{\nu}_\mu W_L^+W_L^-h$ and $\mu^+\mu^- \to \nu_\mu\overline{\nu}_\mu hhh$ at muon colliders are simulated with various energy benchmark points. However, certain p_T cuts in the phase space of final state particles are needed for $pp \to jjW_L^\pm W_L^\pm h$ and $\mu^+\mu^- \to \nu_\mu\overline{\nu}_\mu W_L^+W_L^-h$ processes, in order to reduce the SM cross sections enhanced by Sudakov logarithms from collinear divergences. We study in details on how cross sections change with energies and with the Wilson coefficients c_6 and c_{Φ_1} in figure 8 to figure 11.

JHEP10(2021)099

Based on the simulation, we estimated the allowed regions of c_6 and c_{Φ_1} at different c.m. energies and types of colliders assuming that signal events are already extracted from relevant SM backgrounds for processes in eq. (4.1) and eq. (4.2). Cross sections of these processes are generally tiny at HL-LHC, HE-LHC and CLIC, which makes them very challenging to explore. On the other hand, we find at the future 100 TeV pp colliders or high energy muon colliders, these VBS processes are good processes to measure the Higgs self-couplings, parameterized by c_6 and c_{Φ_1} in SMEFT. The allowed 1-σ and 2-σ regions for c_6 and c_{Φ_1} are obtained based on simple event counting procedure and are summarized in figure 12. Optimistically, we expect $-0.23 < c_6 < 0.18, -0.07 < c_{\Phi_1} < 0.04$ at 1σ can be reached in the future and c_{Φ_1} is more restrictive than c_6.

We find WWh process is as important as the more widely studied triple Higgs production (hhh) [6, 44, 50, 75–84] in the measurement of Higgs self-couplings. Our analysis is only preliminary, as we aim to give an overall picture and qualitative conclusions. A more careful analysis that takes into account of decay products, relevant SM background and detector effects is obviously needed. Moreover, we only studied a partial list of all $2 \to 3$ VBS processes, with $W^\pm W^\pm h/hhh$ (W^+W^-h/hhh) as final states at hadron (lepton) colliders. We will devote a more complete survey for all $2 \to 3$ VBS processes in measuring Higgs self-couplings in future work.

Furthermore, the enhancement of the amplitude at high energy in the presence of BSM physics due to contact scalar vertices is not limited to the case of $2 \to 3$ VBS processes. For example, the analysis in this paper can also be applied to $2 \to 4$ VBS processes which have the same energy increase behavior. Hence, they can also be used to measure Higgs self-coupling at future high energy colliders. It would be interesting to explore further on this direction.

Acknowledgments

We would like to thank helpful discussions with Yang Ma, Tong Li. CTL is supported by KIAS Individual Grant, No.PG075301 at Korea Institute for Advanced Study. JMC is supported by Fundamental Research Funds for the Central Universities of China NO.11620330.

A Full cross sections summing over polarization vector bosons

In this appendix, we sum over polarizations for final state $W^\pm$s of $\mu^+\mu^- \to \nu_\mu \bar{\nu}_\mu W^+W^-h$ and $pp \to jjW^+W^-h$ processes in table 14 and table 15, respectively. Compared with table 2 and table 5, the relevant cross sections can be larger by one order, but the relative deviations from SM ones are not obvious, especially for the c_6 contributions. Therefore, a precise way to distinguish $W_L^\pm$ from $W_T^\pm$ is important to extract effects from the $\mathcal{O}_6$ operator. In this work, we assume $W_L^\pm$ can already be successfully separated from $W_T^\pm$ experimentally. More details about the method to distinguish $W_L^\pm$ from $W_T^\pm$ can be found in [67–71].

Open Access. This article is distributed under the terms of the Creative Commons Attribution License (CC-BY 4.0), which permits any use, distribution and reproduction in any medium, provided the original author(s) and source are credited.

JHEP10(2021)099

Cross sections (pb) for $\mu^+\mu^- \to \nu_\mu \bar{\nu}_\mu W^+W^- h$ with $c_{\Phi_1} = 0$					
c_6	-2	-1	0	1	2
1 TeV	2.87×10^{-8}	2.51×10^{-8}	2.37×10^{-8}	2.44×10^{-8}	2.73×10^{-8}
3 TeV	2.04×10^{-5}	1.90×10^{-5}	1.85×10^{-5}	1.88×10^{-5}	2.01×10^{-5}
5 TeV	8.18×10^{-5}	7.74×10^{-5}	7.60×10^{-5}	7.72×10^{-5}	8.07×10^{-5}
10 TeV	3.16×10^{-4}	3.02×10^{-4}	3.00×10^{-4}	3.02×10^{-4}	3.13×10^{-4}
14 TeV	5.29×10^{-4}	5.12×10^{-4}	5.03×10^{-4}	5.06×10^{-4}	5.29×10^{-4}
30 TeV	1.38×10^{-3}	1.31×10^{-3}	1.31×10^{-3}	1.33×10^{-3}	1.36×10^{-3}

Cross sections (pb) for $\mu^+\mu^- \to \nu_\mu \bar{\nu}_\mu W^+W^- h$ with $c_6 = 0$					
c_{Φ_1}	-2	-1	0	1	2
1 TeV	5.99×10^{-6}	6.85×10^{-6}	7.97×10^{-6}	9.40×10^{-6}	1.11×10^{-5}
3 TeV	2.39×10^{-4}	2.51×10^{-4}	2.81×10^{-4}	3.29×10^{-4}	3.90×10^{-4}
5 TeV	7.15×10^{-4}	7.00×10^{-4}	7.58×10^{-4}	8.96×10^{-4}	1.11×10^{-3}
10 TeV	2.66×10^{-3}	2.12×10^{-3}	2.12×10^{-3}	2.66×10^{-3}	3.69×10^{-3}
14 TeV	5.07×10^{-3}	3.48×10^{-3}	3.15×10^{-3}	4.22×10^{-3}	6.50×10^{-3}
30 TeV	2.49×10^{-2}	1.10×10^{-2}	6.81×10^{-3}	1.25×10^{-2}	2.76×10^{-2}

Table 14. The $\mu^+\mu^- \to \nu_\mu \bar{\nu}_\mu W^+W^- h$ process with summing over polarizations for final $W^\pm$, with different c.m. energies, varies with c_6, $c_{\Phi_1} = 0$ (upper table) and varies with c_{Φ_1}, $c_6 = 0$ (lower table). Same cuts listed in table 3 are applied.

Cross sections (pb) for $pp \to jjW^\pm W^\pm h$ with $c_{\Phi_1} = 0$					
c_6	-2	-1	0	1	2
14 TeV	1.39×10^{-5}	1.37×10^{-5}	1.36×10^{-5}	1.37×10^{-5}	1.42×10^{-5}
27 TeV	9.11×10^{-5}	8.93×10^{-5}	8.91×10^{-5}	8.98×10^{-5}	9.15×10^{-5}
100 TeV	1.13×10^{-3}	1.11×10^{-3}	1.11×10^{-3}	1.12×10^{-3}	1.13×10^{-3}

Cross sections (pb) for $pp \to jjW^\pm W^\pm h$ with $c_6 = 0$					
c_{Φ_1}	-2	-1	0	1	2
14 TeV	2.26×10^{-4}	2.51×10^{-4}	2.83×10^{-4}	3.21×10^{-4}	3.63×10^{-4}
27 TeV	1.04×10^{-3}	1.14×10^{-3}	1.27×10^{-3}	1.46×10^{-3}	1.67×10^{-3}
100 TeV	9.15×10^{-3}	9.48×10^{-3}	1.04×10^{-2}	1.20×10^{-2}	1.42×10^{-2}

Table 15. The same as table 14 for the $pp \to jjW^+W^-h$ process. Same cuts listed in table 3 are applied.

JHEP10(2021)099

References

[1] ATLAS collaboration, *Observation of a new particle in the search for the Standard Model Higgs boson with the ATLAS detector at the LHC*, *Phys. Lett. B* **716** (2012) 1 [arXiv:1207.7214] [INSPIRE].

[2] CMS collaboration, *Observation of a new boson at a mass of* 125 *GeV with the CMS experiment at the LHC*, *Phys. Lett. B* **716** (2012) 30 [arXiv:1207.7235] [INSPIRE].

[3] P.W. Higgs, *Broken symmetries and the masses of gauge bosons*, *Phys. Rev. Lett.* **13** (1964) 508 [INSPIRE].

[4] F. Englert and R. Brout, *Broken symmetry and the mass of gauge vector mesons*, *Phys. Rev. Lett.* **13** (1964) 321 [INSPIRE].

[5] G.S. Guralnik, C.R. Hagen and T.W.B. Kibble, *Global conservation laws and massless particles*, *Phys. Rev. Lett.* **13** (1964) 585 [INSPIRE].

[6] P. Agrawal, D. Saha, L.-X. Xu, J.-H. Yu and C.P. Yuan, *Determining the shape of the Higgs potential at future colliders*, *Phys. Rev. D* **101** (2020) 075023 [arXiv:1907.02078] [INSPIRE].

[7] J. Alison et al., *Higgs boson potential at colliders: status and perspectives*, *Rev. Phys.* **5** (2020) 100045 [arXiv:1910.00012] [INSPIRE].

[8] CMS collaboration, *Search for nonresonant Higgs boson pair production in final states with two bottom quarks and two photons in proton-proton collisions at* $\sqrt{s} = 13$ *TeV*, *JHEP* **03** (2021) 257 [arXiv:2011.12373] [INSPIRE].

[9] ATLAS collaboration, *Search for Higgs boson pair production in the two bottom quarks plus two photons final state in pp collisions at* $\sqrt{s} = 13$ *TeV with the ATLAS detector*, Tech. Rep. ATLAS-CONF-2021-016, CERN, Geneva, Switzerland (2021).

[10] C.-T. Lu, J. Chang, K. Cheung and J.S. Lee, *An exploratory study of Higgs-boson pair production*, *JHEP* **08** (2015) 133 [arXiv:1505.00957] [INSPIRE].

[11] A. Adhikary, S. Banerjee, R.K. Barman, B. Bhattacherjee and S. Niyogi, *Revisiting the non-resonant Higgs pair production at the HL-LHC*, *JHEP* **07** (2018) 116 [arXiv:1712.05346] [INSPIRE].

[12] D. Gonçalves, T. Han, F. Kling, T. Plehn and M. Takeuchi, *Higgs boson pair production at future hadron colliders: from kinematics to dynamics*, *Phys. Rev. D* **97** (2018) 113004 [arXiv:1802.04319] [INSPIRE].

[13] J. Chang, K. Cheung, J.S. Lee, C.-T. Lu and J. Park, *Higgs-boson-pair production* $H(\to bb)H(\to \gamma\gamma)$ *from gluon fusion at the HL-LHC and HL-*100 *TeV hadron collider*, *Phys. Rev. D* **100** (2019) 096001 [arXiv:1804.07130] [INSPIRE].

[14] M. Cepeda et al., *Report from working group* 2*: Higgs physics at the HL-LHC and HE-LHC*, *CERN Yellow Rep. Monogr.* **7** (2019) 221 [arXiv:1902.00134] [INSPIRE].

[15] K. Cheung, A. Jueid, C.-T. Lu, J. Song and Y.W. Yoon, *Disentangling new physics effects on nonresonant Higgs boson pair production from gluon fusion*, *Phys. Rev. D* **103** (2021) 015019 [arXiv:2003.11043] [INSPIRE].

[16] B. Henning, D. Lombardo, M. Riembau and F. Riva, *Measuring Higgs couplings without Higgs bosons*, *Phys. Rev. Lett.* **123** (2019) 181801 [arXiv:1812.09299] [INSPIRE].

[17] F. Maltoni, L. Mantani and K. Mimasu, *Top-quark electroweak interactions at high energy*, *JHEP* **10** (2019) 004 [arXiv:1904.05637] [INSPIRE].

JHEP10(2021)099

[18] J.M. Cornwall, D.N. Levin and G. Tiktopoulos, *Derivation of gauge invariance from high-energy unitarity bounds on the s matrix*, *Phys. Rev. D* **10** (1974) 1145 [*Erratum ibid.* **11** (1975) 972] [INSPIRE].

[19] M.S. Chanowitz and M.K. Gaillard, *The TeV physics of strongly interacting W's and Z's*, *Nucl. Phys. B* **261** (1985) 379 [INSPIRE].

[20] G.J. Gounaris, R. Kogerler and H. Neufeld, *Relationship between longitudinally polarized vector bosons and their unphysical scalar partners*, *Phys. Rev. D* **34** (1986) 3257 [INSPIRE].

[21] S. Weinberg, *Baryon and lepton nonconserving processes*, *Phys. Rev. Lett.* **43** (1979) 1566 [INSPIRE].

[22] W. Buchmüller and D. Wyler, *Effective Lagrangian analysis of new interactions and flavor conservation*, *Nucl. Phys. B* **268** (1986) 621 [INSPIRE].

[23] C.N. Leung, S.T. Love and S. Rao, *Low-energy manifestations of a new interaction scale: operator analysis*, *Z. Phys. C* **31** (1986) 433 [INSPIRE].

[24] CEPC Study Group collaboration, *CEPC conceptual design report: volume 2 — physics & detector*, arXiv:1811.10545 [INSPIRE].

[25] F. An et al., *Precision Higgs physics at the CEPC*, *Chin. Phys. C* **43** (2019) 043002 [arXiv:1810.09037] [INSPIRE].

[26] ILD collaboration, *Measurement of Higgs couplings and self-coupling at the ILC*, *PoS* **EPS-HEP2013** (2013) 316 [arXiv:1311.6528] [INSPIRE].

[27] D.M. Asner et al., *ILC Higgs white paper*, in *Community summer study* 2013*: Snowmass on the Mississippi*, (2013) [arXiv:1310.0763] [INSPIRE].

[28] P. Bambade et al., *The International Linear Collider: a global project*, arXiv:1903.01629 [INSPIRE].

[29] CLIC Physics Working Group collaboration, *Physics at the CLIC multi-TeV linear collider*, in 11$^{\text{th}}$ *international conference on hadron spectroscopy*, *CERN Yellow Repts. Monogr.* **6** (2004) [hep-ph/0412251] [INSPIRE].

[30] A. Robson and P. Roloff, *Updated CLIC luminosity staging baseline and Higgs coupling prospects*, arXiv:1812.01644 [INSPIRE].

[31] CLICdp collaboration, *Double Higgs boson production and Higgs self-coupling extraction at CLIC*, *Eur. Phys. J. C* **80** (2020) 1010 [arXiv:1901.05897] [INSPIRE].

[32] J.P. Delahaye et al., *Muon colliders*, arXiv:1901.06150 [INSPIRE].

[33] K. Long, D. Lucchesi, M. Palmer, N. Pastrone, D. Schulte and V. Shiltsev, *Muon colliders to expand frontiers of particle physics*, *Nature Phys.* **17** (2021) 289 [arXiv:2007.15684] [INSPIRE].

[34] D. Buttazzo, D. Redigolo, F. Sala and A. Tesi, *Fusing vectors into scalars at high energy lepton colliders*, *JHEP* **11** (2018) 144 [arXiv:1807.04743] [INSPIRE].

[35] A. Costantini et al., *Vector boson fusion at multi-TeV muon colliders*, *JHEP* **09** (2020) 080 [arXiv:2005.10289] [INSPIRE].

[36] T. Han, D. Liu, I. Low and X. Wang, *Electroweak couplings of the Higgs boson at a multi-TeV muon collider*, *Phys. Rev. D* **103** (2021) 013002 [arXiv:2008.12204] [INSPIRE].

JHEP10(2021)099

[37] N. Arkani-Hamed, T. Han, M. Mangano and L.-T. Wang, *Physics opportunities of a* 100 *TeV proton-proton collider*, *Phys. Rept.* **652** (2016) 1 [arXiv:1511.06495] [INSPIRE].

[38] H.-J. He, J. Ren and W. Yao, *Probing new physics of cubic Higgs boson interaction via Higgs pair production at hadron colliders*, *Phys. Rev. D* **93** (2016) 015003 [arXiv:1506.03302] [INSPIRE].

[39] A. Azatov, R. Contino, G. Panico and M. Son, *Effective field theory analysis of double Higgs boson production via gluon fusion*, *Phys. Rev. D* **92** (2015) 035001 [arXiv:1502.00539] [INSPIRE].

[40] D. de Florian, I. Fabre and J. Mazzitelli, *Higgs boson pair production at NNLO in QCD including dimension* 6 *operators*, *JHEP* **10** (2017) 215 [arXiv:1704.05700] [INSPIRE].

[41] L.-S. Ling, R.-Y. Zhang, W.-G. Ma, X.-Z. Li, L. Guo and S.-M. Wang, *Dimension-six operators in Higgs boson pair production via vector-boson fusion at the LHC*, *Phys. Rev. D* **96** (2017) 055006 [arXiv:1708.04785] [INSPIRE].

[42] S. Jana and S. Nandi, *New physics scale from Higgs observables with effective dimension-*6 *operators*, *Phys. Lett. B* **783** (2018) 51 [arXiv:1710.00619] [INSPIRE].

[43] J.H. Kim, Y. Sakaki and M. Son, *Combined analysis of double Higgs production via gluon fusion at the HL-LHC in the effective field theory approach*, *Phys. Rev. D* **98** (2018) 015016 [arXiv:1801.06093] [INSPIRE].

[44] F. Maltoni, D. Pagani and X. Zhao, *Constraining the Higgs self-couplings at* e^+e^- *colliders*, *JHEP* **07** (2018) 087 [arXiv:1802.07616] [INSPIRE].

[45] W. Bizoń, U. Haisch and L. Rottoli, *Constraints on the quartic Higgs self-coupling from double-Higgs production at future hadron colliders*, *JHEP* **10** (2019) 267 [arXiv:1810.04665] [INSPIRE].

[46] A. Biekötter, D. Gonçalves, T. Plehn, M. Takeuchi and D. Zerwas, *The global Higgs picture at* 27 *TeV*, *SciPost Phys.* **6** (2019) 024 [arXiv:1811.08401] [INSPIRE].

[47] S. Borowka, C. Duhr, F. Maltoni, D. Pagani, A. Shivaji and X. Zhao, *Probing the scalar potential via double Higgs boson production at hadron colliders*, *JHEP* **04** (2019) 016 [arXiv:1811.12366] [INSPIRE].

[48] G. Li, L.-X. Xu, B. Yan and C.P. Yuan, *Resolving the degeneracy in top quark Yukawa coupling with Higgs pair production*, *Phys. Lett. B* **800** (2020) 135070 [arXiv:1904.12006] [INSPIRE].

[49] M. Capozi and G. Heinrich, *Exploring anomalous couplings in Higgs boson pair production through shape analysis*, *JHEP* **03** (2020) 091 [arXiv:1908.08923] [INSPIRE].

[50] M. Chiesa, F. Maltoni, L. Mantani, B. Mele, F. Piccinini and X. Zhao, *Measuring the quartic Higgs self-coupling at a multi-TeV muon collider*, *JHEP* **09** (2020) 098 [arXiv:2003.13628] [INSPIRE].

[51] J. Bagger and C. Schmidt, *Equivalence theorem redux*, *Phys. Rev. D* **41** (1990) 264 [INSPIRE].

[52] H.G.J. Veltman, *The equivalence theorem*, *Phys. Rev. D* **41** (1990) 2294 [INSPIRE].

[53] Y.-P. Yao and C.P. Yuan, *Modification of the equivalence theorem due to loop corrections*, *Phys. Rev. D* **38** (1988) 2237 [INSPIRE].

[54] H.-J. He, Y.-P. Kuang and X.-Y. Li, *On the precise formulation of equivalence theorem*, *Phys. Rev. Lett.* **69** (1992) 2619 [INSPIRE].

JHEP10(2021)099

[55] H.-J. He, Y.-P. Kuang and X.-Y. Li, *Further investigation on the precise formulation of the equivalence theorem*, *Phys. Rev. D* **49** (1994) 4842 [INSPIRE].

[56] H.-J. He, Y.-P. Kuang and C.P. Yuan, *Equivalence theorem and probing the electroweak symmetry breaking sector*, *Phys. Rev. D* **51** (1995) 6463 [hep-ph/9410400] [INSPIRE].

[57] A. Dedes, W. Materkowska, M. Paraskevas, J. Rosiek and K. Suxho, *Feynman rules for the Standard Model effective field theory in R_ξ-gauges*, *JHEP* **06** (2017) 143 [arXiv:1704.03888] [INSPIRE].

[58] T. Kinoshita, *Mass singularities of Feynman amplitudes*, *J. Math. Phys.* **3** (1962) 650 [INSPIRE].

[59] T.D. Lee and M. Nauenberg, *Degenerate systems and mass singularities*, *Phys. Rev.* **133** (1964) B1549 [INSPIRE].

[60] G.F. Sterman and S. Weinberg, *Jets from quantum chromodynamics*, *Phys. Rev. Lett.* **39** (1977) 1436 [INSPIRE].

[61] G.F. Sterman, *Summation of large corrections to short distance hadronic cross-sections*, *Nucl. Phys. B* **281** (1987) 310 [INSPIRE].

[62] S. Dawson, *The effective W approximation*, *Nucl. Phys. B* **249** (1985) 42 [INSPIRE].

[63] J. Chen, T. Han and B. Tweedie, *Electroweak splitting functions and high energy showering*, *JHEP* **11** (2017) 093 [arXiv:1611.00788] [INSPIRE].

[64] T. Hahn, *Generating Feynman diagrams and amplitudes with FeynArts* 3, *Comput. Phys. Commun.* **140** (2001) 418 [hep-ph/0012260] [INSPIRE].

[65] T. Hahn and M. Pérez-Victoria, *Automatized one loop calculations in four-dimensions and D-dimensions*, *Comput. Phys. Commun.* **118** (1999) 153 [hep-ph/9807565] [INSPIRE].

[66] J. Alwall et al., *The automated computation of tree-level and next-to-leading order differential cross sections, and their matching to parton shower simulations*, *JHEP* **07** (2014) 079 [arXiv:1405.0301] [INSPIRE].

[67] A. Ballestrero, E. Maina and G. Pelliccioli, *W boson polarization in vector boson scattering at the LHC*, *JHEP* **03** (2018) 170 [arXiv:1710.09339] [INSPIRE].

[68] A. Ballestrero, E. Maina and G. Pelliccioli, *Different polarization definitions in same-sign WW scattering at the LHC*, *Phys. Lett. B* **811** (2020) 135856 [arXiv:2007.07133] [INSPIRE].

[69] S. De, V. Rentala and W. Shepherd, *Measuring the polarization of boosted, hadronic W bosons with jet substructure observables*, arXiv:2008.04318 [INSPIRE].

[70] M. Grossi, J. Novak, B. Kersevan and D. Rebuzzi, *Comparing traditional and deep-learning techniques of kinematic reconstruction for polarization discrimination in vector boson scattering*, *Eur. Phys. J. C* **80** (2020) 1144 [arXiv:2008.05316] [INSPIRE].

[71] T. Kim and A. Martin, *A $W^\pm$ polarization analyzer from deep neural networks*, arXiv:2102.05124 [INSPIRE].

[72] C. Degrande, G. Durieux, F. Maltoni, K. Mimasu, E. Vryonidou and C. Zhang, *Automated one-loop computations in the standard model effective field theory*, *Phys. Rev. D* **103** (2021) 096024 [arXiv:2008.11743] [INSPIRE].

[73] M.L. Mangano et al., *Physics at a* 100 *TeV pp collider: standard model processes*, arXiv:1607.01831 [INSPIRE].

JHEP10(2021)099

[74] J. de Blas et al., *Higgs boson studies at future particle colliders*, *JHEP* **01** (2020) 139 [arXiv:1905.03764] [INSPIRE].

[75] C.-Y. Chen, Q.-S. Yan, X. Zhao, Y.-M. Zhong and Z. Zhao, *Probing triple-Higgs productions via $4b2\gamma$ decay channel at a 100 TeV hadron collider*, *Phys. Rev. D* **93** (2016) 013007 [arXiv:1510.04013] [INSPIRE].

[76] B. Fuks, J.H. Kim and S.J. Lee, *Probing Higgs self-interactions in proton-proton collisions at a center-of-mass energy of 100 TeV*, *Phys. Rev. D* **93** (2016) 035026 [arXiv:1510.07697] [INSPIRE].

[77] D.A. Dicus, C. Kao and W.W. Repko, *Self coupling of the Higgs boson in the processes $pp \to ZHHH + X$ and $pp \to WHHH + X$*, *Phys. Rev. D* **93** (2016) 113003 [arXiv:1602.05849] [INSPIRE].

[78] B. Fuks, J.H. Kim and S.J. Lee, *Scrutinizing the Higgs quartic coupling at a future 100 TeV proton-proton collider with taus and b-jets*, *Phys. Lett. B* **771** (2017) 354 [arXiv:1704.04298] [INSPIRE].

[79] P. Agrawal, D. Saha and A. Shivaji, *Production of HHH and $HHV(V = \gamma, Z)$ at the hadron colliders*, *Phys. Rev. D* **97** (2018) 036006 [arXiv:1708.03580] [INSPIRE].

[80] A.S. Belyaev, P.B. Schaefers and M.C. Thomas, *Precise test of Higgs boson properties via triple Higgs boson production in vector boson fusion at future colliders*, *Phys. Rev. D* **99** (2019) 015030 [arXiv:1801.10157] [INSPIRE].

[81] W. Kilian, S. Sun, Q.-S. Yan, X. Zhao and Z. Zhao, *Multi-Higgs boson production and unitarity in vector-boson fusion at future hadron colliders*, *Phys. Rev. D* **101** (2020) 076012 [arXiv:1808.05534] [INSPIRE].

[82] A. Papaefstathiou, G. Tetlalmatzi-Xolocotzi and M. Zaro, *Triple Higgs boson production to six b-jets at a 100 TeV proton collider*, *Eur. Phys. J. C* **79** (2019) 947 [arXiv:1909.09166] [INSPIRE].

[83] D. de Florian, I. Fabre and J. Mazzitelli, *Triple Higgs production at hadron colliders at NNLO in QCD*, *JHEP* **03** (2020) 155 [arXiv:1912.02760] [INSPIRE].

[84] M. Gonzalez-Lopez, M.J. Herrero and P. Martinez-Suarez, *Testing anomalous $H - W$ couplings and Higgs self-couplings via double and triple Higgs production at e^+e^- colliders*, *Eur. Phys. J. C* **81** (2021) 260 [arXiv:2011.13915] [INSPIRE].

JHEP10(2021)099